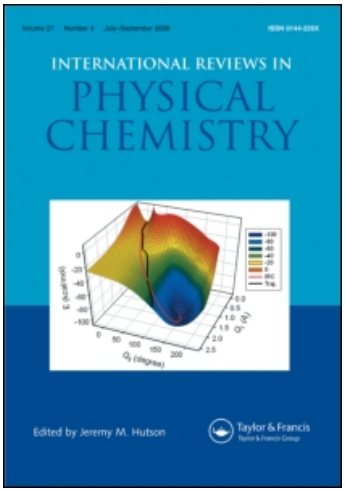

International Reviews in Physical Chemistry
Publication details, including instructions for authors and subscription information:
http://www.informaworld.com/smpp/title~content=t713724383

Quantum non-adiabatic dynamics through conical intersections: Spectroscopy to reactive scattering

Susanta Mahapatra[a]
[a] School of Chemistry, University of Hyderabad, Hyderabad, India

To cite this Article Mahapatra, Susanta(2004) 'Quantum non-adiabatic dynamics through conical intersections: Spectroscopy to reactive scattering', International Reviews in Physical Chemistry, 23: 4, 483 — 512
To link to this Article: DOI: 10.1080/01442350500037455
URL: http://dx.doi.org/10.1080/01442350500037455

INT. REVIEWS IN PHYSICAL CHEMISTRY, 2004
VOL. 23, NO. 4, 483–512

Taylor & Francis
Taylor & Francis Group

Quantum non-adiabatic dynamics through conical intersections: Spectroscopy to reactive scattering

SUSANTA MAHAPATRA*

School of Chemistry, University of Hyderabad, Hyderabad, 500 046, India

Some of the recent developments in the quantum dynamical studies at the conical intersections of molecular potential energy surfaces is briefly reviewed in this article. Particular emphasis is given to a variety of molecular processes studied by us in the recent past. The non-adiabatic effects due both to the electronic as well as relativistic spin–orbit coupling are considered. The discussions include the Jahn–Teller effect (and also the pseudo-Jahn–Teller effect whenever applicable) in the Rydberg emission spectrum of triatomic hydrogen and the photoelectron spectrum of cyclopropane and methyl fluoride, probing the conical intersections in ClO_2 and the reagent van der Waals well in the $Cl(^2P)+H_2$ reaction via the photodetachment spectroscopy of the negative ions, ClO_2^- and ClH_2^-, respectively, and the thermal scattering dynamics of $H+H_2$ and $Cl(^2P)+H_2$ reactions on multisheeted potential energy surfaces.

Contents

PAGE

1. Introduction 484

2. The Jahn–Teller and pseudo-Jahn–Teller conical intersections 486
2.1. The $(E \times e)$-JT interactions in the $1^2E'$ ground electronic manifold of H_3 486
2.2. Multimode $(E \times e)$-JT interactions the cyclopropane radical cation and beyond 488
2.3. $(E + A) \times e$-JT plus PJT effects in CH_3F^+ 492

3. Negative ion photodetachment spectroscopy 494
3.1. Probing the $\widetilde{A}^2B_2$–$\widetilde{B}^2A_1$ conical intersections in ClO_2 495
3.2. Probing the pre-reactive van der Waals resonances in $Cl+H_2$ scattering 499

4. Reactive scattering dynamics 503
4.1. The $H+H_2$ reaction dynamics 503
4.2. The $Cl+H_2$ reaction dynamics 506

5. Summary 508

Acknowledgments 508

References 509

*E-mail: smsc@uohyd.ernet.in

International Reviews in Physical Chemistry ISSN 0144–235X print/ISSN 1366–591X online
http://www.tandf.co.uk/journals
DOI: 10.1080/01442350500037455

1. Introduction

Understanding the nuclear motion on coupled multisheeted electronic potential energy surfaces (PESs) of polyatomic molecular systems appears to be one of the fundamental and challenging problems in chemical dynamics [1]. The double cone topography [referred to as conical intersections (CIs)] of the electronic PESs in the vicinity of crossing is now a fairly well established concept and is recognized to play important mechanistic roles in the spectroscopy of polyatomic molecules, photochemistry and reaction dynamics [2–13]. The book edited by Domcke, Yarkony and Köppel [11] represents an excellent collection of articles in this emerging area of chemical dynamics. CIs of PESs form a $N-2$-dimensional seam – a hyperline, where N represents the total number of vibrational degrees of freedom. Therefore, CIs are characterized by the degeneracy of the two PESs in the $N-2$-dimensional intersection space and a lifting of degeneracy in first-order with respect to nuclear displacements in the two-dimensional branching space [5, 8, 9]. In addition to the electronic coupling when the relativistic spin–orbit (SO) coupling is operating the dimensionality of the branching space has been shown to change to 5 in general and to 3 if C_s symmetry is present [14].

The existence of CIs of PESs causes a breakdown of the adiabatic or Born–Oppenheimer approximation [5, 16], and therefore, electronic transitions take place during nuclear motion. As a result, the mathematical treatment of the nuclear dynamics becomes very cumbersome [5, 11] and difficult as one needs to monitor the nuclear motions simultaneously on more than one PES. Apart from this, a second complexity arises from the diverging nature of part of the non-adiabatic coupling elements, Λ. The latter represent the derivative matrix elements of the electronic wavefunction with respect to the nuclear coordinates in an adiabatic electronic basis [5–7]

$$\Lambda_{ij} = -\int d\mathbf{r}\Phi_i^*(\mathbf{r},\mathbf{R})\big[T_n, \Phi_j(\mathbf{r},\mathbf{R})\big], \tag{1}$$

where Φ represents the electronic states, T_n the nuclear kinetic energy operator and $\mathbf{r}$ and $\mathbf{R}$ collectively denote the electronic and nuclear coordinates, respectively. In terms of the first- and second-order derivative couplings, Λ_{ij} in Cartesian coordinates can be written as [5–7]

$$\Lambda_{ij} = -\sum_k \frac{\hbar^2}{M_k} F_{ij}\frac{\partial}{\partial R_k} - \sum_k \frac{\hbar^2}{2M_k} G_{ij}, \tag{2}$$

where M_k are nuclear masses and

$$F_{ij} = \langle \Phi_i(\mathbf{r})|\nabla_{\mathbf{k}}|\Phi_j(\mathbf{r})\rangle, \tag{3}$$

$$G_{ij} = \langle \Phi_i(\mathbf{r})|\nabla_{\mathbf{k}}^{\mathbf{2}}|\Phi_j(\mathbf{r})\rangle, \tag{4}$$

in which $\nabla_{\mathbf{k}} \equiv \partial/\partial R_k$. The matrix elements F_{ij} can be written according to the Hellmann–Feynman type of relation as [5, 12]

$$F_{ij} = \langle \Phi_i|\nabla|\Phi_j\rangle = \frac{\langle \Phi_i|\nabla H_e(\mathbf{r},\mathbf{R})|\Phi_j\rangle}{V_i(\mathbf{R}) - V_j(\mathbf{R})}, \tag{5}$$

where H_e defines the electronic hamiltonian for fixed nuclear coordinates. When the two surfaces are degenerate, $V_i(\mathbf{R}) = V_j(\mathbf{R})$ and the F_{ij} exhibit singular behaviour. As a result, both the electronic wavefunction and energy become discontinuous at

the seam of CIs making the adiabatic representation unsuitable for dynamical studies.

In order to deal with this situation one resorts to a diabatic electronic representation [17–19] which can be obtained through a suitable unitary transformation of the adiabatic Hamiltonian

$$\mathcal{H}^d = \mathbf{S}\mathcal{H}^{ad}\mathbf{S}^\dagger = T_n\mathbf{1} + \mathbf{W}. \tag{6}$$

Here $\mathbf{S}$ defines the orthogonal transformation matrix. For a 2×2 Hamiltonian, $\mathbf{S}$ is given by

$$\mathbf{S} = \begin{pmatrix} \cos\theta & \sin\theta \\ -\sin\theta & \cos\theta, \end{pmatrix} \tag{7}$$

where θ represents the adiabatic-to-diabatic transformation angle and $\Psi^d = \mathbf{S}\Psi^{ad}$. With this transformation, the diverging kinetic couplings of equation (5) are transformed into the smooth potential coupling (off-diagonal elements of $\mathbf{W}$ in equation 6) and thereby the discontinuity of the adiabatic representation is avoided. Construction of diabatic electronic states for realistic molecular systems is, however, a tedious and difficult problem and various approximate mathematical schemes have been proposed in the literature [20–24] to accomplish this.

A typical dynamical outcome that bears the signature of CIs of PESs is the femtosecond decay of excited molecular states [5, 25]. The corresponding electronic transition reveals seemingly diffuse and overlapping bands that exhibit highly complex and dense line structure under high resolution. On the lower electronic state (adiabatic) the phenomena of the geometric phase [26–28], bifurcation of the wavepacket [29] and dissipative vibrational motions [30] are observed. While the earlier literature on the nuclear dynamics at CIs focused on the spectroscopy of bound molecular systems, the effects of CIs on the thermal reactive scattering have received attention only recently (see, for example, Ref. [31] and references therein). The thermal bimolecular reactive scattering dynamics in the gas phase occurring on the uncoupled ground electronic state of the system has been extensively studied in the literature [32–36]. With the advent of much sophisticated crossed molecular beam techniques a study of the interplay of the electronic and relativistic SO coupling on the bimolecular reactive scattering processes in the gas phase has currently become a newly emerging topic of research in chemical dynamics [37–53].

This review focuses on some of these and related effects due to CIs of PESs in the quantum dynamics of a wide variety of molecular systems studied by us in the recent past with the aid of time-independent and time-dependent quantum mechanical techniques. In order to deal with small-amplitude vibrations in the multisheeted coupled electronic states we extend the originally proposed linear vibronic coupling model of Cederbaum and coworkers [5] constructed in terms of the dimensionless normal coordinates of the molecular system. The large-amplitude vibrations and the scattering processes are described in a body-fixed Jacobi coordinate system. The interplay of electronic and SO coupling effects on the nuclear dynamics and chemical reactivity is also considered and discussed. The physical processes that are considered below include the static and dynamical aspects of the Jahn–Teller (JT) and pseudo-Jahn–Teller (PJT) CIs in Section 2, the photodetachment spectroscopy of bound and scattering systems in Section 3 and the thermal bimolecular reactive scattering in Section 4. Finally summarizing remarks are presented in Section 5.

2. The Jahn–Teller and pseudo-Jahn–Teller conical intersections

A well-known subclass of conically intersecting potential energy surfaces is represented by JT systems [5, 54–63]. The latter are unstable in a spatially degenerate electronic state and distort in such a way as to remove this degeneracy [54]. This instability is mainly responsible for the ensuing non-adiabatic behaviour of the nuclear motion in such systems [5, 55–63]. Another subclass deals with the vibronic interaction between a degenerate and a non-degenerate electronic state, which is also known as the PJT interaction [5, 64–69]. The latter leads to the possibility of multiple multidimensional CIs with different non-adiabatic couplings and highly complex nuclear dynamics. In the following I concentrate on the effect of the prototypical (and historically the classic) $(E \times e)$-JT CIs on the quantum nuclear dynamics of triatomic hydrogen, cyclopropane radical cation and methyl fluoride radical cation. The possible effect of PJT interactions between the neighbouring electronic states on the nuclear dynamics of the latter two systems is also considered and discussed.

2.1. *The $(E \times e)$-JT interactions in the $1^2E'$ ground electronic manifold of H_3*

The $1^2E'$ ground electronic manifold of H_3 is the simplest representative of a $(E \times e)$-JT class of CIs. The latter is directly probed in the measurement of the Rydberg emission spectrum of H_3. The emission from the $n = 3$ Rydberg electronic state of H_3 terminates in the vicinity of the CIs at the D_{3h} equilibrium configuration on its $1^2E'$ ground electronic manifold. This transition is schematically described in figure 1. The cuts of the pertinent PESs are shown along the Jacobi coordinate R for $r = 1.642\ a_0$ and $\gamma = \pi/2$. Here R and r refer to the Jacobi distance of the third H atom from the centre of mass of H_2 and the H_2 internuclear distance, respectively, and γ is the angle between R and r. These PESs exhibit a crossing at $E = 3.089$ eV. It should be noted that this crossing is not an isolated point in space but represents a cut through the conical intersections, the minimum of which occurs at $E = 2.748$ eV. The initial Rydberg electronic state and the wavefunction of H_3 is also included in

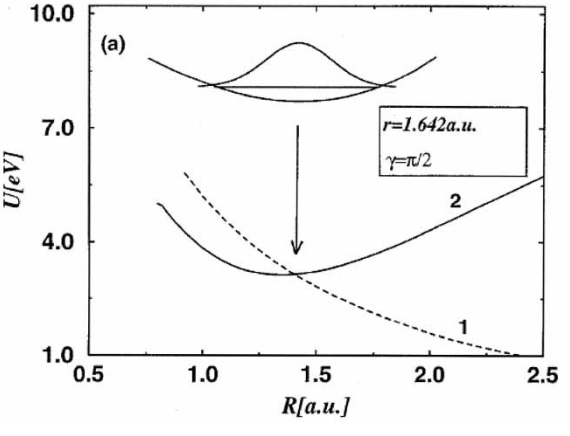

Figure 1. Diabatic potential energies (1 and 2) of the $1^2E'$ ground electronic manifold of H_3 as a function of the Jacobi distance R for fixed values of r and γ indicated in the panel. The Rydberg electronic state and the wavefunction are also shown in the upper part of the figure to illustrate the optical emission process.

the diagram to illustrate the optical emission process. The emission spectra of H_3 and its deuterated isotopomers recorded by Bruckmeier *et al.* [70] revealed highly diffuse and structureless bimodal profiles with two maxima at ~240 nm and ~310 nm. This amounts to a JT splitting of ~9600 cm^{-1} in the $1^2E'$ electronic manifold of H_3. These observations motivated us to undertake a detailed theoretical study to investigate the impact of the CIs on the time-evolution of H_3 in the vicinity of the D_{3h} conformation. In our theoretical approach [71–74] we solved the time-dependent Schrödinger equation numerically in a diabatic electronic representation employing the following two state Hamiltonian:

$$\mathcal{H} = \left(T_N + \frac{V_+ + V_-}{2}\right)\mathbf{1} + \frac{\mathbf{V}_+ + \mathbf{V}_-}{\mathbf{2}} \begin{pmatrix} \cos\alpha & \sin\alpha \\ \sin\alpha & -\cos\alpha \end{pmatrix}. \tag{8}$$

Here T_N stands for the nuclear kinetic energy operator and $V_\pm$ represents the adiabatic sheets of the JT split PES being degenerate at the D_{3h} conformation. The quantity α represents the polar angle in the coordinate space of the two Cartesian components of the degenerate vibrational mode. Within a linear vibronic coupling scheme the angle α can be shown to be twice the so-called adiabatic-to-diabatic mixing angle θ introduced in Section 1 [22]. The above diabatization procedure has been proposed and tested numerically for the first time for a second-order JT problem by Thiel and Köppel [22]. This procedure is shown to remove the leading singular derivative coupling terms of the non-adiabatic coupling matrix Λ [22]. Since α is dependent only on the geometry of the system, a knowledge of the adiabatic PESs alone is sufficient to construct such rigorous diabatic electronic states [22–24]. This procedure is seemingly simple and has a promising future of providing a way to construct diabatic states of complex polyatomic molecular systems [24].

In the nuclear dynamical simulations we used the adiabatic sheets of the double many-body expansion (DMBE) PES of Varandas *et al.* [75] and the set of body-fixed Jacobi coordinates (introduced above) to represent the kinetic energy operator. In figure 1 the cuts represent the diabatic PESs, obtained by diabatizing (as stated above) the adiabatic sheets of the DMBE PES. The theoretically calculated Rydberg emission spectrum of H_3 is shown in figure 2 along with the experimental results of Bruckmeier *et al.* [70]. It can be seen that the theoretical results are in excellent accord with the experimental ones. This also holds for the other deuterated isotopomers of H_3 [72] revealing the accuracy of the DMBE PES as well as the present diabatization procedure at and near the locus of degeneracy. The maxima at ~240 nm and ~310 nm are found to arise from the transition to the lower V_- and upper V_+ adiabatic sheets of the $1^2E'$ electronic manifold, respectively [71]. The two maxima are ~9600 cm^{-1} (~1.2 eV) apart, in good accord with the experimental value of the JT splitting [70]. The JT activity of the degenerate vibrational mode causes the bimodal distribution of the spectral intensity, and the Condon activity of the totally symmetric breathing vibrational mode adds to the diffuseness of the spectrum [73, 74]. The JT effect of the degenerate vibrational mode is particularly strong and as a result the bound vibrational levels of the uncoupled upper adiabatic sheet V_+ transform into highly overlapping resonances when the coupling to the lower sheet is activated [71]. This results into an extremely fast decay of the electronic population of V_+ occurring on a time-scale of ~3–6 fs only [71] for H_3 and all its deuterated isotopomers as shown in figure 3. To the best of our

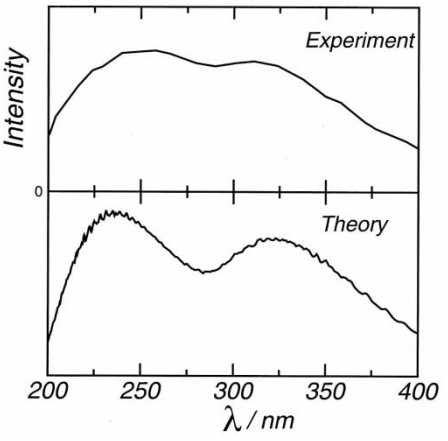

Figure 2. The Rydberg emission spectrum of H_3. The experimental results are reproduced from Ref. [70].

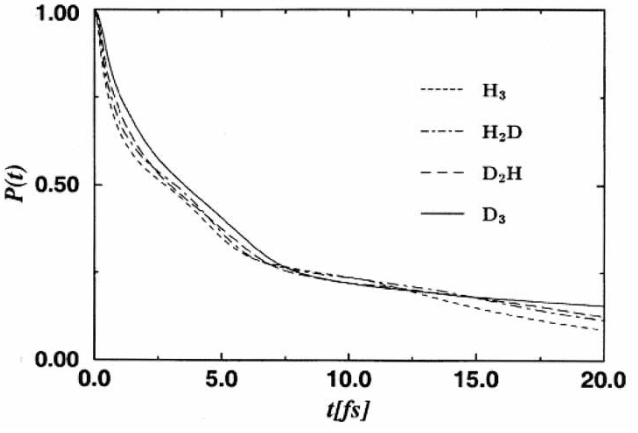

Figure 3. Time dependence of the electronic populations of the upper adiabatic sheet of various isotopomers of H_3 describing the fastest femtosecond decay of molecular states through conical intersections.

knowledge this represents the fastest femtosecond decay process studied in the literature to date.

2.2. *Multimode* ($E \times e$)*-JT interactions the cyclopropane radical cation and beyond*

Cyclopropane (CP) is a fundamental organic hydrocarbon in which the strong interplay between the JT and PJT effects is immediately visible from its photoionization spectrum [76, 77]. The experimental photoelectron spectrum of CP exhibits a bimodal structure centred around ~11 eV, a broad band at ~13.2 eV and two strongly overlapping bands at ~15.7 and ~16.5 eV. The twin band at ~11 eV is due the ionization from the $3e'$ molecular orbital of CP forming its radical cation (CP^+) in the electronic ground $\tilde{X}^2E'$ state. Neutral CP belongs to the D_{3h} symmetry point group at the equilibrium geometry of its electronic ground state.

The elementary symmetry selection rule suggests that its four degenerate vibrational modes of E' symmetry can exhibit the $(E \times e)$-JT activity in the $\widetilde{X}^2E'$ electronic manifold of CP^+. It is interesting to note that the structure of the twin band of CP^+ is quite similar to the bimodal emission profile of H_3 (discussed above) and also the two problems are geometrically analogous. However, in contrast to the single-mode JT activity in H_3, the JT activity in CP^+ is of a multimode nature and highly complex.

The static and dynamic aspects of the multimode JT interactions in the electronic ground manifold of CP^+ have recently been investigated by us at length with the aid of an *ab initio* quantum dynamical method [78]. In our theoretical approach we employed a model diabatic Hamiltonian constructed in terms of the dimensionless normal coordinates (Q_i) of the ground electronic state ($^1A_1'$) of CP within a linear vibronic coupling scheme [5]

$$\mathcal{H} = \mathcal{H}_0\mathbf{1} + \Delta\mathcal{H}. \tag{9}$$

Here $\mathcal{H}_0 = \mathcal{T}_N + \mathcal{V}_0$, with

$$\mathcal{T}_N = -\frac{1}{2}\sum_{i=1}^{3}\omega_i\left(\frac{\partial^2}{\partial Q_i^2}\right) - \frac{1}{2}\sum_{i=4}^{7}\omega_i\left[\frac{\partial^2}{\partial Q_{ix}^2} + \frac{\partial^2}{\partial Q_{iy}^2}\right], \tag{10}$$

$$\mathcal{V}_0 = \frac{1}{2}\sum_{i=1}^{3}\omega_i Q_i^2 + \frac{1}{2}\sum_{i=4}^{7}\omega_i\left(Q_{ix}^2 + Q_{iy}^2\right), \tag{11}$$

is the Hamiltonian matrix associated with the electronic ground state of CP and is defined in terms of unperturbed harmonic oscillators with frequencies ω_i. $\mathbf{1}$ is the (2×2) unit matrix. The dimensionless normal coordinates are calculated by performing geometric optimization of CP in the electronic ground state at the MP2/cc-pVTZ level of theory. The quantity $\Delta\mathcal{H}$ denotes the change in electronic energy upon ionization. This is a (2×2) non-diagonal matrix and its elements represent the interacting (component) diabatic electronic states of CP^+ which are expanded in a Taylor series. Truncation of this series at the linear term leads to the so-called linear vibronic coupling scheme

$$\Delta\mathcal{H} = \begin{pmatrix} E_{E'}^0 + \sum_{i=1}^{3}\kappa_i Q_i + \sum_{i=4}^{7}\lambda_i Q_{xi} & \sum_{i=4}^{7}\lambda_i Q_{yi} \\ \sum_{i=4}^{7}\lambda_i Q_{yi} & E_{E'}^0 + \sum_{i=1}^{3}\kappa_i Q_i - \sum_{i=4}^{7}\lambda_i Q_{xi} \end{pmatrix}. \tag{12}$$

The quantity $E_{E'}^0$ represents the vertical ionization energy of the $\widetilde{X}^2E'$ electronic state of CP^+ computed in the equilibrium geometry ($\mathbf{Q} = \mathbf{0}$) of the ground electronic state of CP. The parameters κ_i and λ_i in the above equation represent the coupling constants (gradients of the adiabatic electronic potential of CP^+ along the normal coordinate of the pertinent vibrational mode evaluated at the equilibrium geometry of the ground electronic state of CP) for the three tuning (A_1' symmetry) and four JT active coupling (E' symmetry) modes, respectively. These are determined by fitting the adiabatic potential energies (equated to the vertical ionization energies from the ground electronic state of CP along the corresponding normal coordinates computed by the outer valence Green's function method) of the $\widetilde{X}^2E'$ electronic manifold of CP^+. The vibronic spectrum

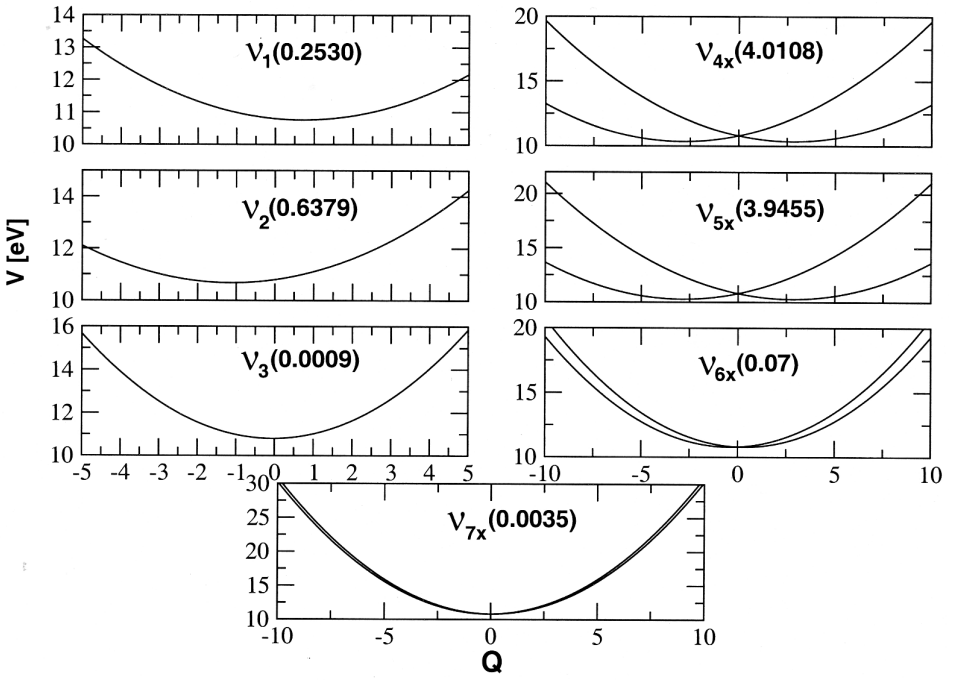

Figure 4. Cuts of the adiabatic potential energy surfaces of the $\widetilde{X}^2E'$ electronic manifold of CP^+ as a function of the dimensionless normal coordinates of the vibrational modes indicated in the panel. The nature of the vibrational modes is explained in the text. The numbers in parentheses indicate the excitation strength, κ^2(or λ^2)/2ω, of the respective mode. The equilibrium geometry of CP in its electronic ground state corresponds to $\mathbf{Q} = 0$.

is calculated by solving the eigenvalue equation with the above Hamiltonian using the Lanczos algorithm.

In figure 4 the cuts of the adiabatic potential energy of the electronic ground state of CP^+ are shown along the dimensionless normal coordinates of the three totally symmetric (A_1'), ν_1 (C–C stretch), ν_2 (CH_2 scissoring), ν_3 (symmetric C–H stretch) and the x-component of the degenerate (E') , ν_4 (CH_2 wagging), ν_5 (ring deformation), ν_6 (CH_2 scissoring) and ν_7 (asymmetric C–H stretch) vibrational modes. These adiabatic potential energy surfaces are obtained by diagonalizing the diabatic electronic Hamiltonian matrix introduced above. The resulting eigenvalues

$$\mathcal{V}_{\mp}(Q) = V_0(Q) + E^0_{E'} + \sum_{i=1}^{3} \kappa_i Q_i \mp \sqrt{\left(\sum_{i=4}^{7} \lambda_i Q_{xi}\right)^2 + \left(\sum_{i=4}^{7} \lambda_i Q_{yi}\right)^2}, \qquad (13)$$

represent the lower ($\mathcal{V}_-$) and upper ($\mathcal{V}_+$) adiabatic sheets of the $\widetilde{X}^2E'$ electronic manifold of CP^+, respectively. The analytic form of the argument of the square root in the above equation represents a *cusp* in the vicinity of the JT undistorted configuration at $\mathbf{Q} = 0$. It can be seen from figure 4 that the three A_1' modes cannot lift the degeneracy of the $\widetilde{X}^2E'$ electronic manifold of CP^+; they only cause a shift of the potential energy minimum of the ionic state compared to that of the neutral and

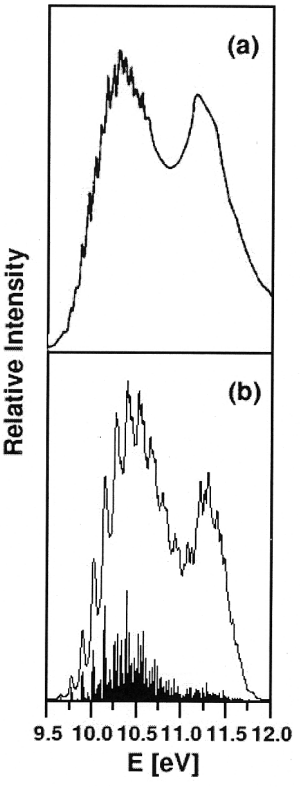

Figure 5. Comparison of experimental [77] (panel a) and final theoretical (linear vibronic coupling model) results for the $\widetilde{X}^2E'$ photoelectron band of CP^+ (panel b) [78].

therefore display tuning activities in the photoelectron spectrum. The degeneracy of the $\widetilde{X}^2E'$ electronic manifold of CP^+, on the other hand, is lifted when distorting along the E' vibrational modes. The activity of a particular vibrational mode in the photoelectron transition depends on its coupling strength ($\kappa^2/2\omega$ or $\lambda^2/2\omega$) given in the parentheses in each panel. It can be seen that the coupling strengths of the ν_3 and ν_7 vibrational modes are very weak compared to the rest and they may be practically disregarded in the dynamical simulations.

The theoretically calculated photoelectron band of the electronic ground state of CP^+ is shown in figure 5 along with the experimental results of Holland and coworkers [77]. The theoretical stick spectrum is calculated by considering the ν_1, ν_2, ν_3, ν_4, ν_5 and ν_6 vibrational modes and is convoluted with a Lorentzian function of 10 meV FWHM to generate the spectral envelope. A careful inspection of the theoretical results revealed the excitation of the C–C stretching (A_1'), CH_2 scissoring (A_1'), CH_2 wagging (E'), ring deformation (E') and CH_2 scissoring (E') vibrational modes in the photoelectron band. It can be seen that the theoretical spectrum is in very good overall agreement with the experimental data. The strong JT activity of the degenerate CH_2 wagging and ring deformation modes leads to the appearance of two distinct maxima in the band indicating transitions to both the sheets of the so-called Mexican hat PES of the $\widetilde{X}^2E'$ electronic manifold. Also, these two modes mainly form the

progression in the low-energy wing of the envelope. The overall width of the band and separation between the two maxima of ~0.76 eV (compared to the experimental value of ~0.78 eV [77]) are reproduced quite well by the linear vibronic coupling model. Despite this overall agreement, the average spacing in the low-energy progression of the band estimated from the theoretical results is ~40 meV higher than the experimental value [77] when the finer details are concerned. This discrepancy is reduced when a quadratic coupling scheme is employed. However, in this case the apparent regularity of the progression is lost [78].

The remaining discrepancies between theory and experiment may be reduced further by including the bilinear coupling terms in the Hamiltonian and considering the possible role of the double prime vibrational modes in the dynamics. The broad and diffuse photoelectron band of CP around ~13.2 eV arises due to the ionization to the first excited $\widetilde{A}^2E''$ electronic manifold of CP^+ [76, 77]. The latter is ~2.43 eV above the ground state in the vertical configuration. The vibrational modes of E' symmetry are also JT active in the $\widetilde{A}^2E''$ electronic manifold and in addition, the double prime vibrational modes can induce PJT crossings between the $\widetilde{X}^2E'$–$\widetilde{A}^2E''$ electronic manifold of CP^+. We have discovered such crossings which are relevant in the energy range of the band [79]. These are also expected to add to the observed diffuseness of the second maxima of the twin band. CP is a rare example where the JT and PJT active vibrational modes are degenerate and have different symmetry. A dynamical study including the JT and PJT interactions and four electronic states is very involved and complex and is presently being carried out.

2.3. $(E + A) \times e$-JT plus PJT effects in CH_3F^+

The equilibrium configuration of methyl fluoride belongs to the C_{3v} symmetry point group. The ground, first and second excited electronic states of the methyl fluoride radical cation belong to the $\widetilde{X}^2E$, $\widetilde{A}^2A_1$ and $\widetilde{B}^2E$ symmetry species in the vertical configuration. In this configuration the $\widetilde{A}^2A_1$ state lies ~3.81 eV above the $\widetilde{X}^2E$ state but is nearly degenerate with the $\widetilde{B}^2E$ state [80]. The three doubly degenerate vibrational modes can exhibit $(E \times e)$-JT activity in the doubly degenerate ground and excited electronic states of the radical cation. The same vibrational modes may also couple the degenerate and the non-degenerate $(\widetilde{A}^2A_1)$ electronic states and can exhibit $(E + A) \times e$ PJT activity. The JT and PJT interactions in the ground and excited electronic states of CH_3F^+ are revealed in the photoelectron spectrum of CH_3F, which indicate resolved vibrational structures at low energies and a highly diffuse and structureless profile at high energies [76, 81].

Very recently, we investigated the static and dynamic aspects of the JT and PJT interactions in the ground and excited electronic manifold of CH_3F^+ with the aid of an *ab initio* quantum dynamical approach [80]. We employed a three-state model diabatic Hamiltonian [5, 66] in which the JT interactions within the E electronic manifold have been modelled with a linear-plus-quadratic (neglecting the bilinear coupling terms) vibronic coupling scheme, and a linear coupling scheme is used for the PJT interactions between the E and A electronic states. The Condon activity of the totally symmetric vibrational modes is described by considering coupling terms up to second order and the interactions between the two E states are neglected [80]. In order to deal with the vibronic dynamics in the E–A interacting manifold of electronic states for this example it is convenient to resort to a complex basis

representation for the degenerate electronic states and complex coordinates for the degenerate vibrational modes. These are defined by

$$\begin{aligned} |\Phi^{+}\rangle &= \frac{1}{\sqrt{2}}(|\Phi^{x}\rangle + i|\Phi^{y}\rangle), \\ |\Phi^{-}\rangle &= \frac{1}{\sqrt{2}}(|\Phi^{x}\rangle - i|\Phi^{y}\rangle), \\ Q_{+} &= Q_{jx} + iQ_{jy} = \rho_j e^{i\phi_j}, \\ Q_{-} &= Q_{jx} - iQ_{jy} = \rho_j e^{-i\phi_j}, \end{aligned} \tag{14}$$

where $|\Phi^{x}\rangle$ and $|\Phi^{y}\rangle$ are the real components of the E electronic manifold; the magnitude and the phase angle of a degenerate vibration j are defined by ρ_j and ϕ_j, respectively. Such a change of representation takes advantage of the three-fold rotational symmetry of the system and the problem becomes computationally less intensive than the same in a Cartesian coordinate system [5]. In this representation the diabatic vibronic Hamiltonian takes the form

$$\widetilde{\mathcal{H}} = \widetilde{\mathcal{H}}_0 \mathbf{1} + \Delta\widetilde{\mathcal{H}}, \tag{15}$$

with

$$\widetilde{\mathcal{H}}_0 = \frac{1}{2}\sum_{j=1}^{3}\omega_j\left(-\frac{\partial^2}{\partial Q_j^2} + Q_j^2\right) + \frac{1}{2}\sum_{j=4}^{6}\omega_j\left(-\frac{1}{\rho_j}\frac{\partial}{\partial\rho_j}\rho_j\frac{\partial}{\partial\rho_j} - \frac{1}{\rho^2}\frac{\partial^2}{\partial\phi_j^2} + \rho_j^2\right), \tag{16}$$

and

$$\Delta\widetilde{H} = \begin{pmatrix} \left(\begin{matrix} E_E^0 + \sum_{j=1}^{3}\kappa_j Q_j \\ + \sum_{j=1}^{3}\gamma_j Q_j^2 + \sum_{j=4}^{6}\gamma_j\rho_j^2 \end{matrix}\right) & \frac{1}{\sqrt{2}}\sum_{i=4}^{6}\lambda'_j\rho_j e^{i\phi_j} & \sum_{j=4}^{6}\lambda_j\rho_j e^{-i\phi_j} + \sum_{j=4}^{6}\eta_j\rho_j^2 e^{2i\phi_j} \\ \frac{1}{\sqrt{2}}\sum_{j=4}^{6}\lambda'_j\rho_j e^{-i\phi_j} & \left(\begin{matrix} E_{A_1}^0 + \sum_{j=1}^{3}\kappa'_j Q_j \\ + \sum_{j=1}^{3}\gamma'_j Q_j^2 + \sum_{j=4}^{6}\gamma'_j\rho_j^2 \end{matrix}\right) & \frac{1}{\sqrt{2}}\sum_{i=4}^{6}\lambda'_j\rho_j e^{i\phi_j} \\ \sum_{j=4}^{6}\lambda_j\rho_j e^{i\phi_j} + \sum_{j=4}^{6}\eta_j\rho_j^2 e^{-2i\phi_j} & \frac{1}{\sqrt{2}}\sum_{j=4}^{6}\lambda'_j\rho_j e^{-i\phi_j} & \left(\begin{matrix} E_E^0 + \sum_{j=1}^{3}\kappa_j Q_j \\ + \sum_{j=1}^{3}\gamma_j Q_j^2 + \sum_{j=4}^{6}\gamma_j\rho_j^2 \end{matrix}\right) \end{pmatrix}, \tag{17}$$

The parameters of the above Hamiltonian have the following physical meaning. The vertical ionization energies of the E and A_1 electronic states of CH_3F^+ are designated as E_E^0 and $E_{A_1}^0$, respectively. The linear intrastate coupling constants for the totally symmetric vibrational modes are given by κ_j and κ'_j in the E and A_1 electronic states, respectively. The linear JT coupling constants for the degenerate vibrational modes in the E electronic state are denoted as λ_j. The quantities λ'_j define

the linear PJT coupling constants for the degenerate vibrational modes which couple the E and A_1 electronic states. The diagonal second-order coupling parameters for the mode j are represented by γ_j and γ_j' in the E and A_1 electronic states, respectively. The quantity η_j represents the quadratic JT coupling parameter in the E electronic manifolds. The quantity Q_j represents the dimensionless normal coordinate of CH_3F associated with the jth vibrational mode of harmonic vibrational frequency ω_j. These parameters of the Hamiltonian are derived by performing extensive *ab initio* calculations at the CASSCF-MR-AQCC level of theory. The adiabatic potential energy surfaces of CH_3F^+ are calculated as a function of the normal coordinates of vibrational modes and the resulting energies are fitted to the mentioned electronic Hamiltonian in the adiabatic form to extract the parameters (see Ref. [80] for details).

The photoelectron bands are calculated with the above Hamiltonian by solving the eigenvalue equation using the Lanczos algorithm. A careful analysis of the results [80] revealed the following physical characteristics. The JT activity of the degenerate vibrational modes is found to be weak in both the $\widetilde{X}^2E$ and $\widetilde{B}^2E$ electronic states of CH_3F^+. With the exception of some details, the agreement between the theoretical and experimental results on the overall structure of the photoelectron bands at low and high energies due to the $\widetilde{X}^2E$ and $\widetilde{B}^2E$ electronic states of the radical cation, respectively, is satisfying [80]. The resolved vibrational structure at low energies is caused by the C–F stretching (A_1), CH_3 deformation (E) and C–F bending (E) vibrational modes in accord with the experimental [76, 81] and previous theoretical results [81]. Although the $\widetilde{X}^2E$ and $\widetilde{A}^2A_1$ states are ~3.81 eV apart in the vertical configuration, still the PJT activity of the C–F bending (E) vibrational mode is found to have a significant effect on the $\widetilde{X}^2E$ photoelectron band at low energies [80]. It is found that a linear-plus-quadratic ($E \times e$)-JT model is clearly inadequate in describing the observed diffuse and structureless appearance of the $\widetilde{B}^2E$ band at high energies. The Condon activity of the C–F stretching (A_1) and the JT activity of the CH_3 deformation (E) modes dominates in the nuclear dynamics of the latter electronic manifold. The linear PJT coupling strengths of the CH_3 deformation (E) and C–F bending (E) vibrational modes in the $\widetilde{A}^2A_1$–$\widetilde{B}^2E$ electronic manifold are nearly identical and small. However, these electronic states are nearly degenerate and therefore even a relatively weak coupling can have significant effects on the nuclear dynamics on them. This is demonstrated in figure 6 from which one can see a huge effect of increasing the line density in the spectrum originating from the PJT interactions (cf. theoretical results in panels b and c). Furthermore, we note that the excitation strengths of the totally symmetric vibrational modes (except C–H stretch) is very large in the non-degenerate $\widetilde{A}^2A_1$ electronic state. Therefore strong multimode effects in the $\widetilde{A}^2A_1$–$\widetilde{B}^2E$ electronic manifold significantly contribute to the diffuse and structureless appearance of the band [80].

3. Negative ion photodetachment spectroscopy

Negative ion photodetachment spectroscopy is a tool to investigate the vibronic structure of neutral electronic states by photodetaching its stable anion [83–88]. This technique has been found to be successful in probing the CIs of excited electronic states [89–97], transition states [98, 99] and the pre-reactive van der Waals wells [100, 101] in chemical reactions. Our recent theoretical studies in support of the experimental data in establishing a conical intersection in the $^2B_2$–$^2A_1$ electronic

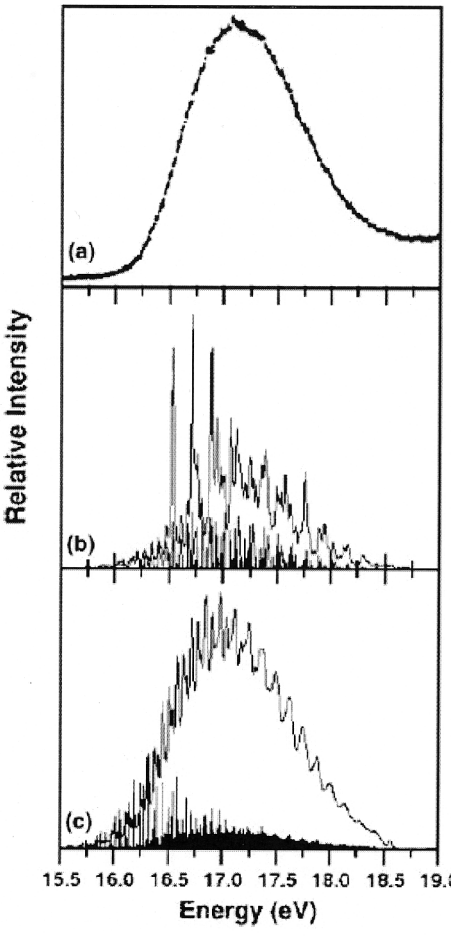

Figure 6. Comparison of experimental [81] (panel a) superposition of uncoupled $\widetilde{B}^2E$ and $\widetilde{A}^2A_1$ bands (panel b) and final theoretical results with JT and PJT coupling in the $\widetilde{A}^2A_1$–$\widetilde{B}^2E$ electronic manifold of CH_3F^+ (panel c).

states of ClO_2 and a van der Waals well in the reagent asymptote of the $Cl(^2P)+H_2$ reaction are discussed below.

3.1. *Probing the $\widetilde{A}^2B_2$–$\widetilde{B}^2A_1$ conical intersections in ClO_2*

The photochemistry of chlorine dioxide is a subject of outstanding complexity. The decline in the stratospheric ozone layer catalysed by atmospheric chlorine has drawn considerable interest in the complex structural and dynamical properties of this species [102]. The photochemistry and fragmentation dynamics of ClO_2 has been a subject of debate, and both experimental and theoretical studies have predicted the involvement of two intermediate near-degenerate electronic states of $^2B_2$ and $^2A_1$ symmetry in defining the photoproducts [103, 104]. According to these, a direct dissociation of the $^2A_2$ state leads to the production of ClO+O and an internal conversion of the $^2A_2$ state to the $^2A_1$ state mediated by the SO coupling followed by the non-radiative decay to the $^2B_2$ state (driven by the $^2B_2$–$^2A_1$ vibronic coupling) leads to the production of ClO+O or $Cl+O_2$ [103–107]. Even though the crucial roles

of the $^2B_2$ and $^2A_1$ electronic states have been anticipated in the photochemistry of ClO_2, their existence remained unconfirmed experimentally for a long time! They cannot be probed in an optical absorption experiment because the $^2B_2$ state is optically dark and the $^2A_1 \leftarrow \widetilde{X}^2B_1$ transition has extremely low oscillator strength [108]. Although indirect evidence of the existence of a $^2A_1$ state emerged from combined experimental and theoretical studies on the resonance Raman spectrum of OClO [109], the existence of a $^2B_2$ state solely relied on theoretical predictions [105–107]. Recently Sun *et al.* have revisited the femtosecond pump-probe photodissociation of OClO and demonstrated direct observation of a very weak signal due to the $^2A_1$ state [110]. Unlike optical absorption spectroscopy, photodetachment spectrocopy is not constrained by any selection rule [83–95]. The photodetachment experiment by Gilles *et al.* probed the ground electronic $\widetilde{X}^2B_1$ state of the neutral OClO for the first time [111]. Later, Wang and Wang [96] recorded the photodetachment spectrum of ClO_2^- with increasing photon energy and observed the appearance of a diffuse and highly overlapping band structure in the 4.0–5.5 eV electron binding energy range. This structure is predicted to be due to the ionization of ClO_2^- to the $^2B_2$, $^2A_1$ and $^2A_2$ electronic states of ClO_2 [96].

In order to understand the observed diffuse structure of the photodetachment spectrum and to add to the evidence in favour of the existence of a $^2B_2$ state in ClO_2, we devised a theoretical model and simulated the nuclear dynamics on coupled multiple electronic states with the aid of a time-dependent wavepacket approach [97]. We extended the near-equilibrium *ab initio* C_{2v} PESs of Peterson and Werner [105–107] to C_s configurations assuming a harmonic vibration along the asymmetric stretch coordinate. A symmetry-allowed CI between the $^2B_2$ and $^2A_1$ electronic states in the vicinity of the Franck–Condon zone for the photodetachment process is established [97]. The topography of this CI is shown in figure 7, where the potential energies of the two diabatic electronic states, $^2B_2(H_{11})$ and $^2A_1(H_{22})$, are plotted as contour lines for the C_{2v} configuration of ClO_2 and shown by the thin and thick

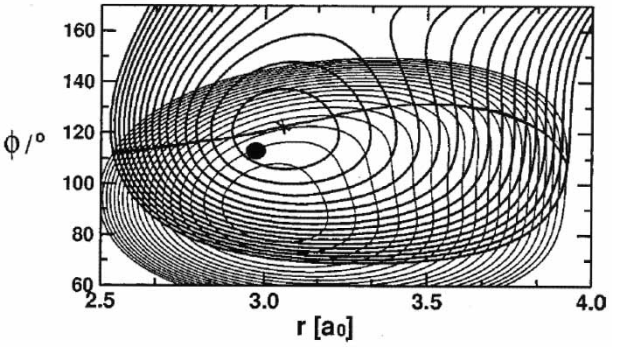

Figure 7. Contour line drawing of the $^2B_2$ (thin solid lines) and $^2A_1$ (thick solid lines) potential energy surfaces of ClO_2 for the C_{2v} configuration. The diabatic potential energies are plotted as a function of C–O bond length r and O–Cl–O angle ϕ. The minimum energy contours in the diagram occur at 0.2 eV and 0.8 eV for the $^2B_2$ and $^2A_1$ states, respectively, and the spacing between successive contour lines is 0.2 eV. The zero of energy corresponds to the minimum of the $^2B_2$ state. The seam of conical intersections between these states is shown by the solid line, and the cross on it indicates its energetic minimum. The heavy dot on the diagram indicates the centre of the Franck–Condon zone of the photodetachment process.

solid lines, respectively. The seam of conical intersections of these two states is shown by the solid line and the cross on it indicates its energetic minimum. The heavy dot on the diagram indicates the centre of the Franck–Condon (FC) zone in the photodetachment process. The intersection seam occurs closer to the equilibrium geometry of the $^2A_1$ state and located relatively far away from the equilibrium geometry of the $^2B_2$ state. Therefore, the motion of the wavepacket (WP) on the $^2A_1$ state is expected to be more perturbed by the associated non-adiabatic coupling, whereas the latter will have relatively less impact on the low-lying vibronic structure of the $^2B_2$ state. The strength of the linear vibronic coupling parameter λ between these two states is calculated by performing *ab initio* calculations and found to vary between 0.018 and 0.114 eV [97]. We note that λ is not a constant quantity and depends on the nuclear coordinates. The mentioned variation in the magnitude of λ reveals this property.

The SO interactions between the $^2A_1$ and $^2A_2$ is estimated to be weak ($\sim 2\,cm^{-1}$) [109] and is not considered in the dynamical simulations. The calculations are carried out in a diabatic electronic representation and the theoretical results are presented along with the 157 nm experimental recording of Wang and Wang [96] in figures 8(a,b). The results obtained with harmonic (approximated to a stationary Gaussian wavepacket (GWP) located at the equilibrium geometry of the anionic

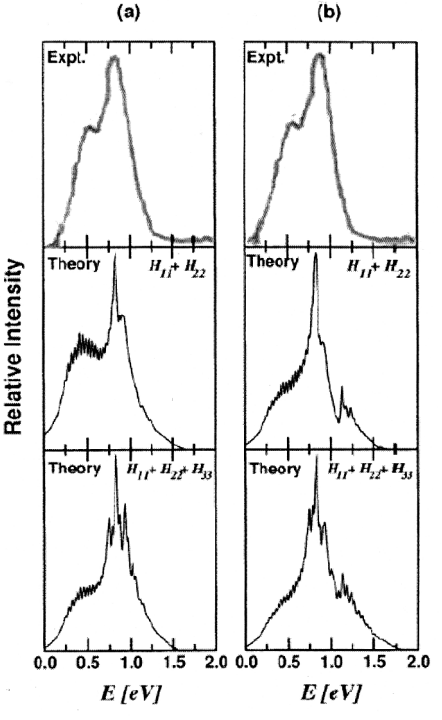

Figure 8. The composite photodetachment spectrum obtained with (a) a harmonic and (b) an anharmonic initial wavefunction of ClO_2^- (see text) corresponding to a transition to the low-lying excited electronic states H_{11}, H_{22} and H_{33} ($^2B_2, ^2A_1$ and $^2A_2$, respectively in the C_{2v} configuration). The 157 nm experimental spectrum is reproduced from Ref. [96] and shown in the upper panel.

ground state) and anharmonic (calculated with the aid of a relaxation scheme using the potential energy surface of the anionic ground electronic state [105–107]) anionic wavefunctions are shown in figures 8(a) and 8(b), respectively. The theoretical results obtained by considering the $^2B_2$ and $^2A_1$ electronic states and their coupling only are presented in the middle panel of each figure. These results are combined with the uncoupled surface results of the $^2A_2$ electronic state and are presented in the bottom panel of figures 8(a,b). A careful inspection of the theoretical results reveals that the humplike structure at low energies corresponds to the vibronic structure of the $^2B_2$ electronic state and the diffuse structure at high energies corresponds to that of the $^2A_1$ and $^2A_2$ electronic states of ClO_2 [97]. When combining the theoretical results presented in the bottom panel, we assumed a 100% contribution to the spectral intensity from the $^2A_2$ electronic states. However, a close look at the theoretical results of the middle panels suggests a small contribution of the $^2A_2$ electronic states to the spectral intensity when compared with experiment [96]. This is in line with the estimated low magnitude of the SO coupling between the $^2A_1$–$^2A_2$ states [109].

The time dependence of the adiabatic (thin solid lines) and diabatic (thick solid lines) electronic populations derived from the coupled $^2B_2$–$^2A_1$ electronic states is shown in figure 9. The two curves in the upper part of the panel represent the populations of the states correlating with the $^2B_2$ species, whereas the two in the lower part of the panel represent the populations of the states correlating with the $^2A_1$ species. The initial WP is located on the H_{22} ($^2A_1$) diabatic electronic state and the population of this state is 1.0 at $t=0$. In about ~50 fs the population of both diabatic states reaches a value of 0.5. The population of the H_{22} state rapidly decreases to within 100 fs, then exhibits quasi-periodic oscillations. These oscillations are damped and the population fluctuates around a value of ~0.3 at longer times. The population of the H_{11} diabatic state on the other hand grows from a value of 0.0 at $t=0$ and fluctuates statistically around a value of 0.7 at longer times. Since the adiabatic states represent an admixture of the diabatic electronic states, the population of the lower (upper) adiabtic sheet is 3% (97%) at $t=0$. The population of the lower (upper) adiabatic sheet reaches a value of 0.8 (0.2) at longer times. It can be seen that with increasing time ~80% of the WP moves on to the lower

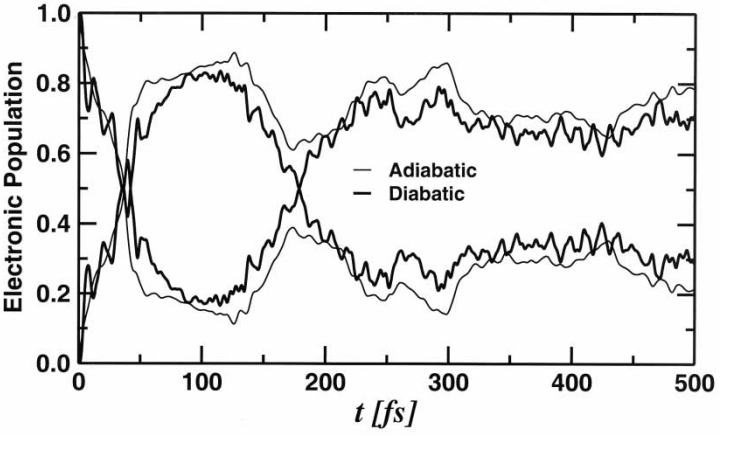

Figure 9. Time dependence of the adiabatic (thin solid lines) and diabatic (thick solid lines) electronic populations derived from the $^2B_2$–$^2A_1$ coupled state dynamics of ClO_2.

adiabatic sheet and remains there and consequently the nuclear dynamics is by and large governed by the topography of this sheet. Both the diabatic and adiabatic populations reach their equilibrium values only after ~250 fs, therefore the major portion of the population exchange between these states takes place within this time. This estimate is in excellent agreement with the recent time-resolved experimental findings of Stert *et al.* [112] revealing the reliability of the estimated strength of λ. The overall satisfying agreement between the experimental and theoretical results bears strong evidence in favour of the existence of a $^2B_2$ electronic state in ClO_2 and establishes its CIs with the next higher electronic state of $^2A_1$ symmetry.

3.2. *Probing the pre-reactive van der Waals resonances in Cl+H_2 scattering*

The photodetachment technique is successfully applied to examine the spectroscopy of the transition state in the exothermic F+H_2 reaction [98, 99, 113–115]. The equilibrium geometry of the FH_2^- anion is closer to the barrier configuration in the neutral F+H_2 ground electronic PES. Therefore, a FC transition of the anion to the neutral PES could directly probe this barrier region and unravel the structure of the reactive transition state [113–115]. In contrast, the simplest Cl atom reaction Cl+H_2 is slightly endothermic (endothermicity ~0.045 eV) and proceeds on a late barrier type of PES (barrier height ~0.366 eV) [52]. The geometry of ClH_2^- is considerably stretched and is far away from the barrier configuration but is close to the van der Waals well region of the reactive Cl+H_2 PES [116]. The latter is probed by photodetachment spectroscopy which provides the first experimental evidence in favour of the existence and importance of a shallow van der Waals well in the reagent asymptote of a reactive potential energy surface [100, 101].

The dynamics of the Cl+H_2 reaction in the ground electronic state is perturbed by the electronic and SO coupling with the excited electronic states. The approach of a Cl(^2P) atom to the H_2 molecule splits the three-fold degeneracy of the ^2P state. This leads to three adiabatic electronic states with $^2\Sigma_{1/2}$, $^2\Pi_{3/2}$ and $^2\Pi_{1/2}$ symmetries in collinear geometries ($1^2A'$, $1^2A''$ and $2^2A'$ symmetries, respectively, in non-collinear geometries). In the reagent arrangement, the first two states correlate to the ground $^2P_{3/2}$ SO state of the atomic Cl and the third state correlates to its excited $^2P_{1/2}$ SO state. The two $^2A'$ states are electronically coupled to each other and form CIs in the linear geometry. In the product arrangement, the $^2\Sigma_{1/2}$ adiabatic state correlates with the electronic ground state of the products, HCl($\tilde{X}^1\Sigma^+$)+H(^2S), whereas the other two states (the components of the $^2\Pi$ state) correlate with the products in the electronic excited state, HCl($^3\Pi$)+H(^2S). The latter two states are adiabatically closed at low and moderate collision energies and can yield products HCl($\tilde{X}^1\Sigma^+$)+H(^2S) only via non-adiabatic transitions to the $^2\Sigma_{1/2}$ electronic state.

The photodetachment process of ClH_2^- is schematically drawn in figure 10. The adiabatic PESs of the ground electronic state of ClH_2^- and the ground and excited SO states of ClH_2 are plotted as a function of the Jacobi distance R for $r = 1.402a_0$ and the collinear arrangements of the three nuclei. The ground vibrational wavefunction of the anion is also shown in the diagram. This vibrational wavefunction is calculated using the anionic electronic potential of Alexander [116] and a Lanczos based relaxation scheme. We note that the van der Waals well corresponds to a T-shaped configuration of ClH_2 with $R \sim 5.78a_0$, whereas the equilibrium

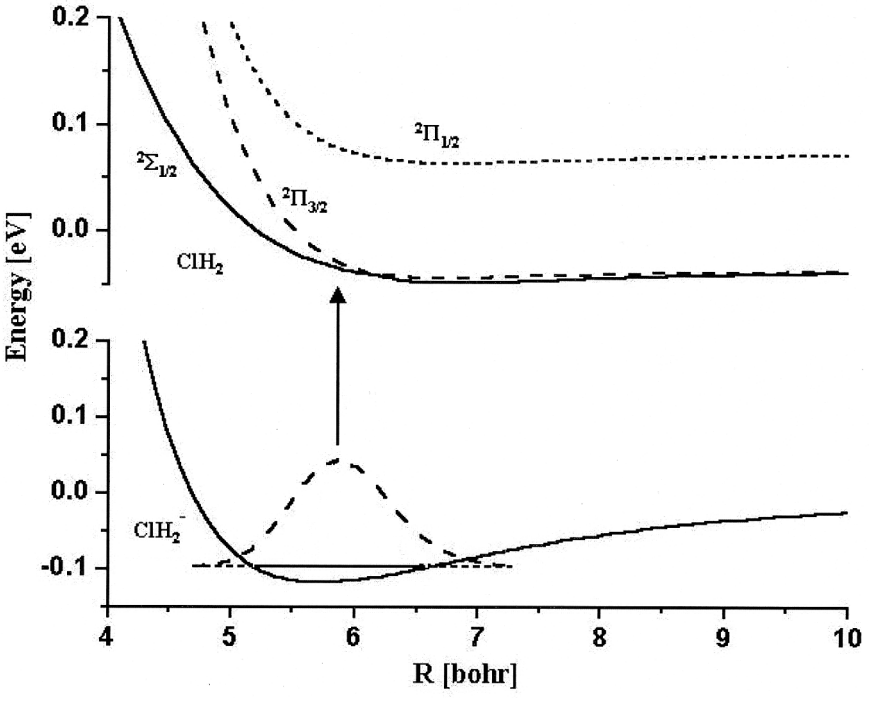

Figure 10. Schematic representation of the adiabatic potential energy surfaces of the ground electronic state of ClH_2^- (solid line in the lower part) and the $^2\Sigma_{1/2}$, $^2\Pi_{3/2}$ and $^2\Pi_{1/2}$ SO states of ClH_2 (in the upper part) along the Jacobi distance R for $r = 1.402a_0$ and $\gamma = 0^\circ$. The initial wavefunction of the anion is shown by the dashed lines in the lower part of the drawing.

geometry of the anion is linear and occurs at a stretched configuration at $R \sim 5.714a_0$. Despite this large difference between the equilibrium geometry of the anion and the location of the van der Waals well on the neutral PESs along the angle γ, the anionic wavefunction is very broad along the angle and its amplitude covers a substantial range of γ.

Based on a time-dependent wavepacket and the coupled *ab initio* SO states of the neutral ClH_2 [52] we investigated the photodetachment dynamics of ClH_2^- [117] employing the following three-state diabatic Hamiltonian:

$$\mathcal{H} = \mathcal{H}^{Nu}\mathbf{1} + \begin{pmatrix} V_\Sigma & -V_1 - i\sqrt{2}B & V_1 \\ -V_1 + i\sqrt{2}B & V_\Pi + A & V_2 \\ V_1 & V_2 & V_\Pi - A \end{pmatrix}, \tag{18}$$

where $\mathcal{H}^{Nu}$ represents the nuclear part of the Hamiltonian which in terms of the Jacobi coordinates in a body-fixed frame is given by

$$\mathcal{H}^{Nu} = -\frac{\hbar^2}{2\mu}\left[\frac{\partial^2}{\partial R^2} + \frac{\partial^2}{\partial r^2}\right] + \frac{\boldsymbol{j}^2}{2I} + \frac{(\boldsymbol{J}^2 + \boldsymbol{L}^2)}{2\mu R^2} - \frac{2\boldsymbol{J}.\boldsymbol{L} + 2\boldsymbol{J}.\boldsymbol{j} - 2\boldsymbol{j}.\boldsymbol{L}}{2\mu R^2}, \tag{19}$$

where $\mu = \sqrt{m_{Cl}m_H^2/(m_{Cl} + 2m_H)}$ (m_{Cl} and m_H being the mass of the Cl and the H atom, respectively) is the three-body uniform reduced mass and $I = \mu R^2 r^2/(R^2 + r^2)$ is the three-body moment of inertia. The first term in equation (19) represents the

radial kinetic energy operators along R (the Cl–H_2 distance) and r (the H–H distance). The various angular momentum terms appearing in the above equation are denoted following the work of Rebentrost and Lester [119–121], Schatz and coworkers (see, for example, Ref. [45, 47, 48]) and Alexander and coworkers [42, 43]. The total electronic angular momentum of the atom is denoted by $\boldsymbol{L}$ ($= \boldsymbol{l} + \boldsymbol{s}$; $\boldsymbol{l}$ and $\boldsymbol{s}$ being the electronic orbital and spin angular momentum with l and s being the associated quantum number, respectively) with L being the corresponding quantum number. The total (electronic + nuclear) angular momentum is denoted by $\boldsymbol{J}$ with corresponding quantum number J. $\boldsymbol{j}$ denotes the diatomic rotational angular momentum, with j being the corresponding quantum number. The rotational kinetic energy operator of the diatom $\boldsymbol{j}^2/2I$, depending on the Jacobi angle γ (angle between $\vec{R}$ and $\vec{r}$), is expressed by the second term of equation (19). The body-fixed projection quantum number associated with $\boldsymbol{j}$, $\boldsymbol{L}$ and $\boldsymbol{J}$ may be denoted as Ω_j, Ω_L and Ω_J, respectively. With the present choice of the body-fixed z-axis, $\Omega = \Omega_j + \Omega_L$.

The calculations reported here are carried out for the lowest value of the total angular momentum $\mathbf{J} = 0.5$ and considering both the electronic and SO couplings. The Coriolis coupling terms are ignored. The final theoretical results obtained with the initial wavefunction of ClH_2^- (cf. figure 10) are presented in figure 11 along with the experimental results of Neumark and coworkers [100, 101]. The theoretical calculations are carried out by considering the initial transition of the anion to each of the three (diabatic) SO states of ClH_2 (cf. figure 10). The resulting three coupled-state spectra are combined together in order to generate the final theoretical results. The theoretical results are in very good accord with experiment; the two large peaks are ~0.102 eV apart when compared with the experimental value of ~0.111 eV and correspond to the SO splittings of ~0.109 eV of the Cl atom. The widths of the individual peaks are also of comparable magnitude. The two satellite peaks (one at low energy and the other in between the large peaks) has been found to get intensities mostly from the transition to the $^2\Pi_{1/2}$ state of ClH_2. Neumark and coworkers [100, 101] have, however, attributed them to be due to the detachment of Cl^- and $Cl(H_2)_2^-$ [100, 101]. Despite this, a detailed analysis revealed that the individual peak structures are quite complex and each peak originates from highly overlapping transitions to all the SO states of ClH_2.

An examination of the fine structures under each peak revealed van der Waals progression (motion along the Cl...H_2 coordinate) as well as progression along the ClH_2 bending motion and H_2 vibration. This is illustrated by plotting the eigenfunction of two typical peaks in the (R, r) and (γ, R) plane in figures 12(a,b). The probability density ($|\Psi|^2$) of the eigenfunctions averaged over γ and r are plotted as contour line diagrams in figures 12(a) and 12(b), respectively. It can be seen from the plots that the wavefunctions exhibit extended progressions along the R (van der Waals) and γ (bending) coordinates revealing the feature of continuum states. We found that the SO coupling effects are particularly strong which cause a splitting of each individual peak of the uncoupled state into two in the coupled state situation. The electronic coupling arising from the $^2\Sigma - ^2\Pi$ CIs has a relatively mild effect on the dynamics [117, 118]. This coupling causes a shift of the energy eigenvalues of the peaks by an amount ~0.035 eV in the coupled state situation. This shift in energy eigenvalue arises due to the geometric phase change of the adiabatic electronic wavefunction while encircling the $^2\Sigma$–$^2\Pi$ CI in a closed loop. These are illustrated by plotting the energy eigenvalue spectra in figure 13, obtained by using the

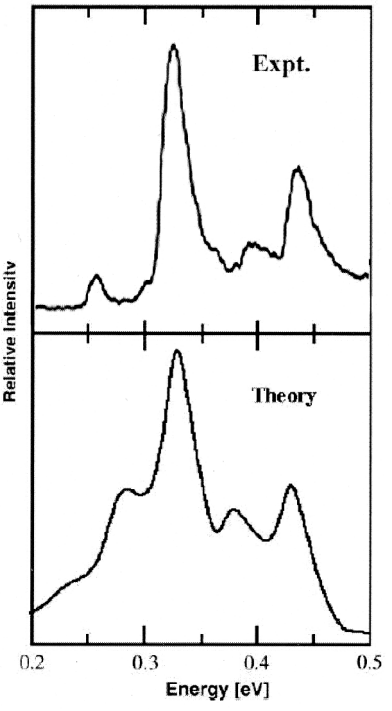

Figure 11. The 299 nm experimental photodetachment spectrum of ClH_2^- reproduced from Ref. [100] along with the coupled-states time-dependent wavepacket results of Ref. [117, 118].

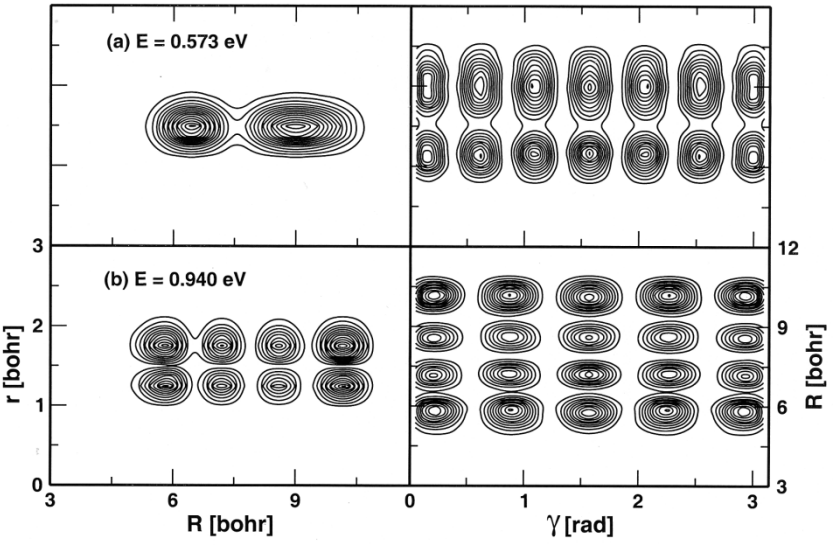

Figure 12. Probability density ($|\Psi|^2$) contours of the quasi-bound eigenfunctions of the $^2\Sigma_{1/2}$ adiabatic electronic state of ClH_2. The energy eigenvalues of the states are indicated in the respective panel and the contours are plotted in the (R, r) and (γ, R) planes for average values of γ and r, respectively.

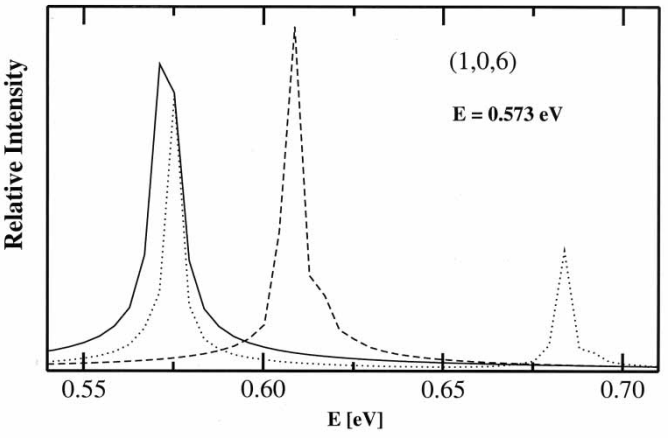

Figure 13. Impact of the electronic and electronic plus SO coupling on the eigenstate (of energy 0.573 eV) of the $^2\Sigma_{1/2}$ adiabatic electronic state of ClH_2. The spectra obtained by propagating this eigenstate in the uncoupled (solid line) and coupled [electronic only (dashed line) and electronic plus SO (dotted line)] state situations are shown in the figure.

eigenfunction of the peak at ~0.573 eV as initial wavefunction in the uncoupled and coupled state situations. The peak shown by the solid line is obtained by propagating this state on the uncoupled $^2\Sigma_{1/2}$ adiabatic state. The peaks shown by the dashed and dotted lines are obtained in the coupled state situations with electronic (only) and electronic plus SO couplings, respectively. The two peak maxima in the latter situation are ~0.112 eV apart (cf. the dotted lines) and this splitting amounts to the SO coupling of the atomic Cl plus the shift due to the electronic coupling as stated above.

In summary, the results of this study corroborate the experimental evidence in favour of the existence of a van der Waals well in a reactive system. This in turn also reveals the spectroscopic accuracy of the *ab initio* PESs [52] of this benchmark system. We note that a FC simulation of this photodetachment spectrum using the same PESs (without considering the coupling surfaces) has been reported very recently [122], which is also shown to be in good accord with the observed spectrum within the experimental energy resolution.

4. Reactive scattering dynamics

4.1. *The $H+H_2$ reaction dynamics*

The prototypical hydrogen exchange reaction $H+H_2 \rightarrow H_2+H$ is one of the cornerstones in our understanding of the microscopic details of chemical reaction dynamics. This reaction proceeds on the degenerate $1^2E'$ electronic manifold of the system. The impact of the CIs of the JT split $1^2E'$ electronic manifold of $H+H_2$ on its reaction dynamics has recently been investigated by us with the aid of a quantum flux operator formalism and a time-dependent wavepacket approach [31, 123]. The reactive scattering process occurs on the repulsive lower adiabatic sheet of this JT-split ground electronic manifold. The upper adiabatic sheet supports bound states in the absence of non-adiabatic coupling to the lower one [71]. The possible impact of the CIs on the reactive scattering dynamics of $H+H_2$ has been studied in

the literature in terms of the geometric phase change of the adiabatic electronic wavefunction [124–126]. Very recently, the role of CIs on the H+H_2 scattering has been demonstrated by computing wavepackets and visualizing them at different times around the D_{3h} conformation [127]. In our approach we explicitly considered both the sheets of the degenerate ground electronic state of H_3 and their coupling in order to investigate the reaction dynamics. This in a way extends the previous studies on this system by going to higher energies and incorporating the geometric phase effects and the non-adiabatic coupling in a coherent fashion. The initial wavefunction pertinent to the H+H_2 reacting system is located in the asymptotic reactant channel on the repulsive lower adiabatic sheet of the DMBE PES and then propagated in a diabatic representation as illustrated above in the case of the Rydberg emission study. The final analysis is carried out by representing the flux operator both in the adiabatic and in the diabatic electronic representations [123].

The energy-dependent reaction probability in a two-state diabatic electronic representation is given by

$$P_i^R(E) = \frac{\hbar}{\mu} \sum_{k=1}^{2} \mathrm{Im}\left[\left\langle \phi_k^d(R, r_d, \gamma, E) \middle| \frac{\partial \phi_k^d(R, r_d, \gamma, E)}{\partial r} \right\rangle \right]\Bigg|_{r=r_d}. \tag{20}$$

The corresponding equation in the adiabatic electronic representation reads

$$\begin{aligned} P_i^R(E) = \frac{\hbar}{\mu} \Bigg[& \mathrm{Im}\left\langle \phi_-^{ad}(R, r_d, \gamma, E) \middle| \frac{\partial \phi_-^{ad}(R, r_d, \gamma, E)}{\partial r} \right\rangle . \\ & + \mathrm{Im}\left\langle \phi_+^{ad}(R, r_d, \gamma, E) \middle| \frac{\partial \phi_+^{ad}(R, r_d, \gamma, E)}{\partial r} \right\rangle \\ & + 2\mathrm{Im}\langle \phi_-^{ad}(R, r_d, \gamma, E) | \alpha_r' | \phi_+^{ad}(R, r_d, \gamma, E) \rangle \Bigg]. \end{aligned} \tag{21}$$

The functions ϕ in the above equations represent the energy-normalized time-independent reactive scattering wavefunction calculated along the dividing surface (between the reactants and products) at $r = r_d$. The flux operator is diagonal in a diabatic basis; however, it contains off-diagonal electronic contributions in an adiabatic electronic basis [123]. Therefore, the reaction probability expression in the latter basis contains off-diagonal terms which are expected to play an important role when both channels, corresponding to V_- and V_+, are open. If only V_- is open then only the first of the three terms on the right-hand side of equation (21) contributes to the reaction probability. Even in this case, however, both terms in the diabatic analogue of equation (20) may play a role, because adiabatic and diabatic surfaces need not coincide asymptotically. In numerical applications both these representations are expected to yield identical results.

The total reaction probability as a function of total energy E for the H+H_2 exchange reaction for $\mathbf{J} = 0$ is shown in figure 14. The solid line indicates the coupled surface results and the long- and short-dashed lines represent the results obtained with the uncoupled lower adiabatic sheet with and without the diagonal correction to the adiabatic Hamiltonian [26], respectively. The energy distribution of the initial translational wavepacket is shown in the inset. The minimum of the seam of CIs

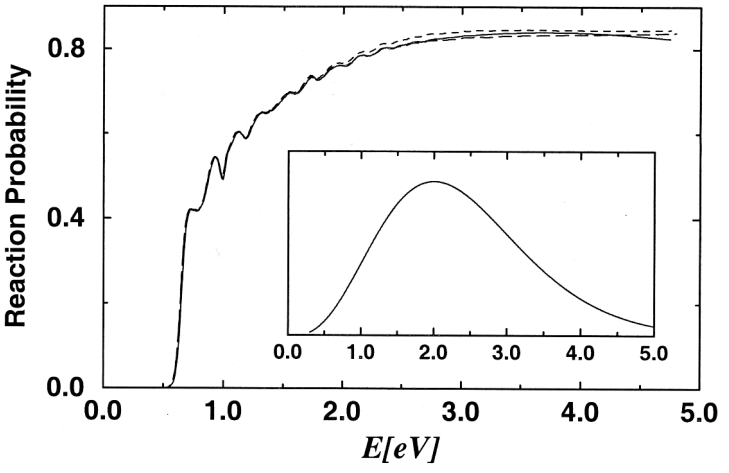

Figure 14. Total reaction probability for the $H+H_2(v=0,j=0) \rightarrow H_2(\sum v', \sum j')+H$ exchange reaction in three dimensions and for total angular momentum $J=0$, plotted as a function of total energy E (H,H_2 translational + H_2 ro-vibrational). The energy E is measured relative to the H_2 potential minimum. The coupled-surface results are shown by the solid line. The uncoupled-surface results with (long-dashed lines) and without (short-dashed lines) the diagonal correction are also shown. The energy distribution of the initial translational wavepacket is shown in the inset.

occurs at ~2.74 eV on the DMBE PES [75]. It can be seen from figure 14 that the reaction probabilities for $H_2(v=0,j=0)$ differ only slightly from the uncoupled surface results beyond this energy, which can be essentially reproduced by adding the diagonal correction term to the single-surface adiabatic Hamiltonian (long-dashed lines). The reaction probability calculated with equations (20) and (21) yield identical values and it is found that the second and the third terms of equation (21) do not contribute to the reaction probability in the energy range of the present investigations. This is because, on the upper adiabatic surface, the product H_2 is formed in its $^3\Sigma_u$ electronic state which has its minimum at $E \sim 4.74$ eV. An analysis of the electronic populations in the coupled state situation revealed [31, 123] that only ~0.625% of the wavepacket reaches the upper adiabatic cone during the course of the entire dynamics. This is shown in figure 15 where the diabatic and adiabtic electronic populations calculated in the coupled state dynamics of the $H+H_2(v=0,j=0)$ reaction are plotted as a function of time. Since the initial wavefunction is prepared on the lower adiabatic electronic state, 71% and 29% populations are obtained on the two component diabatic states at $t=0$. The inset shows the population of the upper adiabatic sheet during the course of the reaction, which reaches a maximum value of $\sim 6.25 \times 10^{-3}$ after ~15 fs.

The fact that the minimum energy path of the $H+H_2$ exchange process occurs at the collinear configuration, and the seam of CIs occurs at the D_{3h} configuration, the CIs do not have any major impact on its reactive scattering dynamics for the lowest value of the total angular momentum [31, 123]. The classical barrier height of the collinear saddle point on the lower adiabatic sheet is ~0.42 eV, whereas the minimum of the seam of conical intersections occurs at ~2.74 eV at the equilateral triangular configuration. Apparently, also for higher energies a major part of the reactive flux is directed via the low-energy collinear transition state conformation.

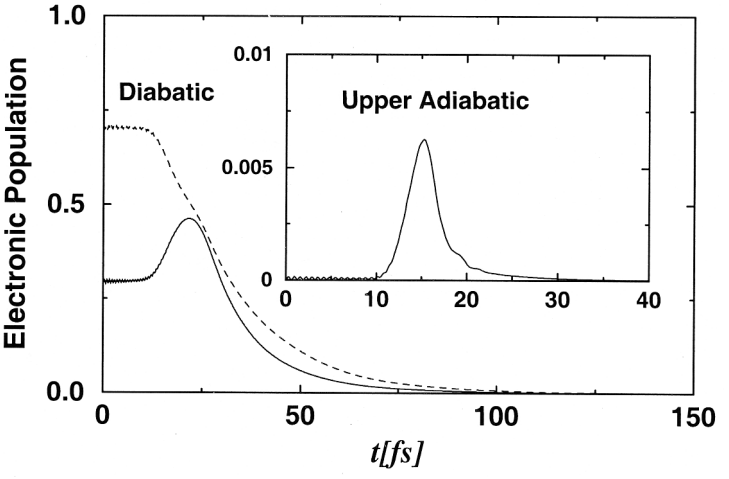

Figure 15. Time dependence of the electronic populations in the coupled state dynamics of the $H+H_2(v=0, j=0) \rightarrow H_2(\sum v', \sum j')+H$ exchange reaction in three dimensions and for total angular momentum $J=0$.

The region of the space covered by the configurations of the three nuclei for which the two surfaces are nearly degenerate is very small and any slight deviation from these configurations leads to a significant energy splitting (~1.2 eV) of the two surfaces.

Unlike in the above situation, where the surface couplings have been found to have only a minor impact on the scattering dynamics, they may have quite significant roles in other situations, e.g., in the $H+O_2$ (see Ref. [49] and Ref. [128]), $N+O_2$ [129, 130] reaction dynamics. Inclusion of the coupling between the two low-lying $^1A'$ electronic states resulted in cross-sections in better agreement with experiment in the $H+O_2$ reaction dynamics. The $N+O_2$ reaction appears to be far more complex and a study of the dynamics of this reaction including the surface coupling effects is expected to yield valuable results and add to the understanding of non-adiabatic reactive scattering dynamics.

4.2. *The Cl+H$_2$ reaction dynamics*

The $Cl+H_2$ reaction dynamics has been a subject of numerous theoretical and experimental investigations in recent years (see, Refs. [40, 41, 52, 53] and references therein). The higher reactivity of SO excited $Cl^*(^2P_{1/2})$ observed in Liu's experiment remains theoretically unresolved to date [131]. Over the years many improved electronic potential energy surfaces have been reported for the system. Most recently, Werner and coworkers have developed the PESs including the electronic and the relativistic SO couplings [52]. Dynamical studies to calculate reaction probabilities and cross-sections have been performed on this surface using time-independent quantum mechanical techniques [40, 41, 53].

The reaction path of the $Cl+H_2$ system is schematically drawn in figure 16 for the collinear arrangements of the three nuclei. The nature of various SO states shown above is discussed in Section 3.2. It can be seen that the reaction on the $^2\Sigma_{1/2}$ electronic state proceeds through a barrier and the reaction is slightly endothermic. The shallow van der Waals well in the reagent asymptote (left side of the diagram) is

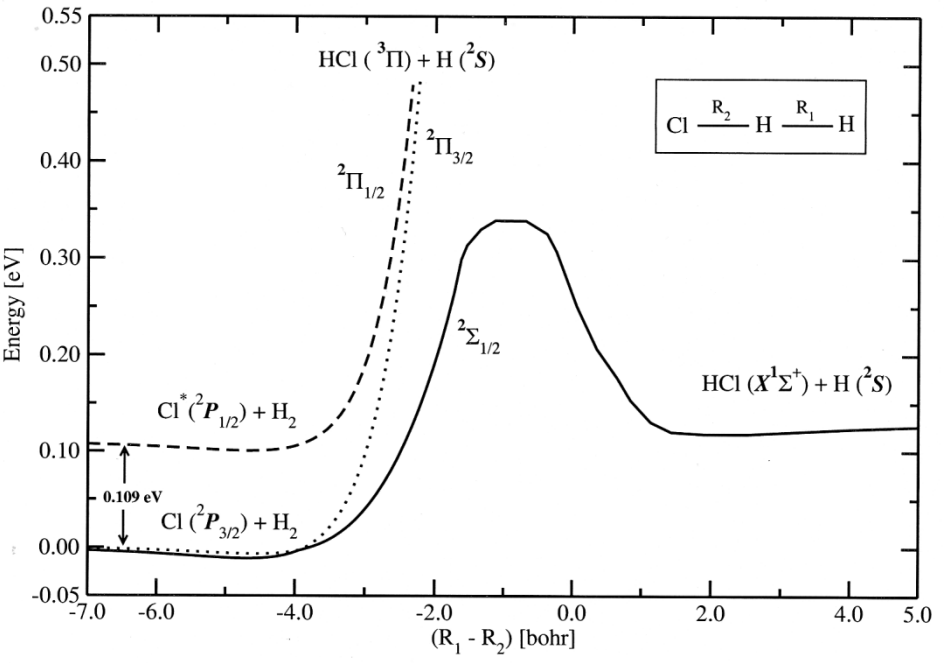

Figure 16. Schematic drawing of the collinear reaction path of the Cl+H_2 system. Shown are the two SO states and their energetic splitting ~0.109 eV. The reagent and product asymptotes are also marked in the figure.

also visible in the plot. The minimum of this well (~0.5 kcal mol^{-1}) occurs at a T-shaped geometry of the three nuclei [52]. The components of the $^2\Pi$ electronic state lead to the product HCl in its $^3\Pi$ electronic state at high energies. They can form the ground state products only via non-adiabatic transitions to the $^2\Sigma_{1/2}$ electronic state.

Following our work on the H+H_2 reactive scattering we extended our flux operator formalism for three electronic states with electronic and SO coupling within a time-dependent wavepacket approach and applied it recently to the realistic case of Cl+H_2 reaction dynamics [132] for the lowest value of the partial wave $\mathbf{J} = 0.5$. To the best of our knowledge this situation is rigorously treated for the first time in a time-dependent picture using coupled three-states consisting of six diabatic surfaces [132]. The excited SO states, viz., $^2\Pi_{3/2}$ and $^2\Pi_{1/2}$, are non-reactive in the adiabatic limit. However, the existence of Σ–Π CIs induces some reactivity of these states via the $^2\Sigma_{1/2}$ state. The probability of the Cl(^2P)+H_2($v = 0, j = 0$)→HCl($\sum v', \sum j'$)+H reaction on the $^2\Sigma_{1/2}$ diabatic electronic state is shown in figure 17. The results obtained with the coupled three-states model including the electronic plus SO coupling is shown by the solid line. The dots superimposed on it represent the probability obtained with the SO coupling alone. The probability obtained with the electronic coupling alone for $\mathbf{J} = 0$ is shown as the dashed line. We note here that the probability results for the uncoupled $^2\Sigma_{1/2}$ diabatic electronic state are exactly equal to the latter. Therefore, the results of figure 17 reveal a huge impact of the SO coupling on the reaction dynamics. The electronic coupling due to the CIs on the other hand has only a minor impact on the dynamics of the $^2\Sigma_{1/2}$ diabatic

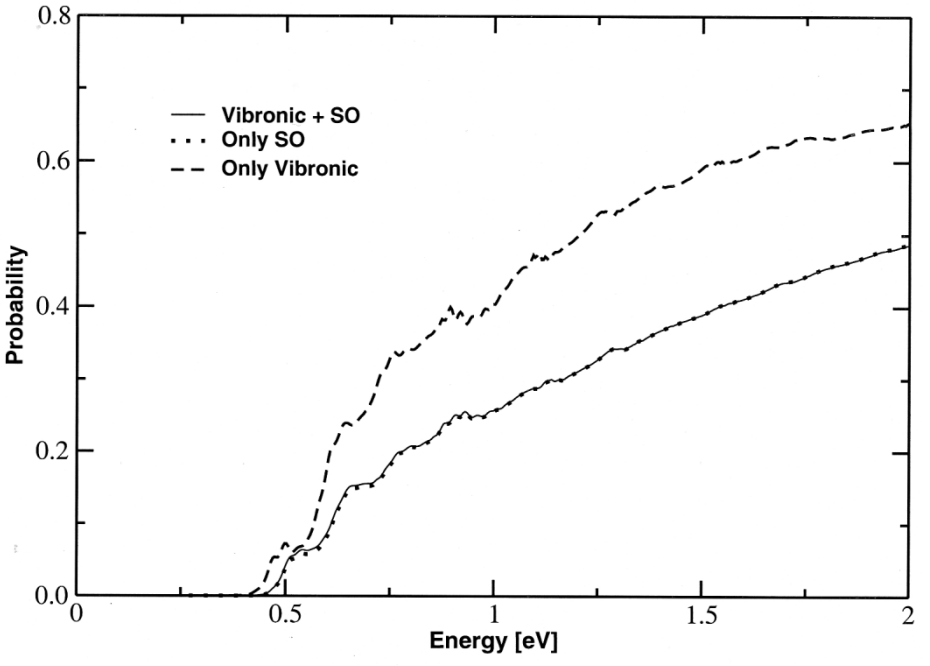

Figure 17. Total reaction probability for the $Cl(^2P)+H_2(v=0,j=0) \rightarrow HCl(\sum v', \sum j')+H$ exchange reaction (see text for further details).

electronic state. Analysis of the reactivity of different SO states revealed that the Π state reacts via the non-adiabatic transition to the $^2\Sigma_{1/2}$ state and is mostly mediated by the Σ–π SO coupling. The SO excited $Cl^*(^2P_{1/2})$ is less reactive compared to its SO ground state, in agreement with the available theoretical results [40, 41, 53] but in apparent contradiction with experiment [131].

5. Summary

A concise account of the quantum dynamics at CIs of PESs of state-of-the-art molecular systems is presented with examples from a wide variety of molecular processes with increasing complexity ranging from spectroscopy to reactive scattering. The spectroscopic probing of the CIs of PESs is discussed. The interplay of the electronic and SO coupling in the quantum molecular dynamics has been considered and treated. Multimode effects, a huge increase in the spectral line density and the ultrafast non-radiative decay of the excited molecular states due to the non-adiabatic coupling associated with the CIs of PESs are delineated.

Acknowledgments

It is a pleasure to acknowledge fruitful collaborations with Professors H. Köppel, L. S. Cederbaum, W. Domcke, Drs. C. Woywod and V. Vallet and with Mrs. T. S. Venkatesan, S. Ghosal and G. M. Krishnan on various topics discussed in this review. Financial support from the AvH Stiftung (Germany), VW Stiftung (Germany) and the DST (New Delhi), CSIR (New Delhi) is gratefully

acknowledged. Thanks also to the UGC, New Delhi, for the computational facilities provided in the University of Hyderabad under the UPE program.

References

[1] *Faraday Discuss.*, **127** (2004).
[2] Teller, E., 1937, *J. Phys. Chem.*, **41**, 109.
[3] Herzberg, G., and Longuet-Higgins, H. C., 1963, *Discuss. Farad. Soc.*, **35**, 77.
[4] Longuet-Higgins, H. C., 1975, *Proc. Roy. Soc. (London) Ser. A*, **344**, 147.
[5] Köppel, H., Domcke, W., and Cederbaum, L. S., 1984, *Adv. Chem. Phys.*, **57**, 59.
[6] Lengsfield, B. H., and Yarkony, D. R., 1992, *Adv. Chem. Phys.*, **82**, 1.
[7] Domcke, W., and Stock, G., 1997, *Adv. Chem. Phys.*, **100**, 1.
[8] Bernardi, F., Olivucci, M., and Robb, M. A., 1996, *Chem. Soc. Rev.*, **25**, 321.
[9] Yarkony, D. R., 1998, *Acc. Chem. Res.*, **31**, 511.
[10] "Conical intersections in photochemistry, spectroscopy and chemical dynamics", 2000, *Chem. Phys.*, **259**.
[11] Domcke, W., Yarkony, D. R., and Köppel, H., (Eds), 2004, in *Conical Intersections: Electronic Structure, Dynamics and Spectroscopy* (Singapore: World-Scientific).
[12] Worth, G. A., and Cederbaum, L. S., 2004, *Ann. Rev. Phys. Chem.*, **55**, 127.
[13] Worth, G. A., and Robb, M. A., 2002, *Adv. Chem. Phys.*, **124**, 355.
[14] Matsika, S., and Yarkony, D. R., 2002, *J. Phys. Chem. B*, **106**, 8108.
[15] Born, M., and Oppenheimer, R., 1927, *Ann. Phys.*, **84**, 457.
[16] Born, M., and Huang, K., 1954, *Dynamical Theory of Crystal Lattices – App. VIII* (Oxford: Oxford University Press).
[17] O'malley, T. F., 1967, *Phys. Rev.*, **162**, 98.
[18] Lichten, W., 1967, *Phys. Rev.*, **164**, 131.
[19] Smith, F. T., 1969, *Phys. Rev.*, **179**, 111.
[20] Baer, M., 1975, *Chem. Phys. Lett.*, **35**, 112.
[21] Pacher, T., Cederbaum, L. S., and Köppel, H., 1993, *Adv. Chem. Phys.*, **84**, 293.
[22] Thiel, A., and Köppel, H., 1999, *J. Chem. Phys.*, **110**, 9371.
[23] Köppel, H., Gronki, J., and Mahapatra, S., 2001, *J. Chem. Phys.*, **115**, 23771.
[24] Köppel, H., 2004, in *Conical Intersections: Electronic Structure, Dynamics and Spectroscopy*, edited by W. Domcke, D. R. Yarkony, and H. Köppel (Singapore: World-Scientific), p. 429.
[25] Köppel, H., and Domcke, W., 1998, in *Encyclopedia of Computational Chemistry*, edited by P. v. R. Schleyer (New York: Wiley), p. 3166.
[26] Mead, C. A., 1992, *Rev. Mod. Phys.*, **64**, 51.
[27] Kendrick, B. K., 2003, *J. Phys. Chem. A*, **107**, 6739.
[28] Kendrick, B. K., 2004, in *Conical Intersections: Electronic Structure, Dynamics and Spectroscopy*, edited by W. Domcke, D. R. Yarkony and H. Köppel (Singapore: World-Scientific), p. 521.
[29] Müller, H., and Köppel, H., 1994, *Chem. Phys.*, **183**, 107.
[30] Schneider, R., Domcke, W., and Köppel, H., 1990, *J. Chem. Phys.*, **92**, 1045.
[31] Mahapatra, S., 2004, in *Conical Intersections: Electronic Structure, Dynamics and Spectroscopy*, edited by W. Domcke, D. R. Yarkony and H. Köppel (Singapore: World-Scientific), p. 555.
[32] Balakrishnan, N., Kalyanaraman, C., and Sathyamurthy, N., 1997, *Phys. Rep.*, **280**, 79.
[33] Mahapatra, S., Chakrabarti, N., and Sathyamurthy, N., 1999, *Int. Rev. Phys. Chem.*, **18**, 235.
[34] Nyman, G., and Yu, H.-G., 2000, *Rep. Prog. Phys.*, **63**, 1001.
[35] Zhang, J. Z. H., 1999, *Theory and Application of Quantum Molecular Dynamics* (Singapore: World Scientific).
[36] Althorpe, S. C., and Clary, D. C., 2003, *Ann. Rev. Phys. Chem.*, **54**, 493.
[37] Liu, K., 2001, *Ann. Rev. Phys. Chem.*, **52**, 139.
[38] Liu, K., 2001, *Int. Rev. Phys. Chem.*, **20**, 189.
[39] Cassavecchia, P., 2000, *Rep. Prog. Phys.*, **63**, 355.

[40] Balucani, N., Skouteris, D., Capozza, G., Segoloni, E., Cassavecchia, P., Alexander, M. H., Capecchi, G., and Werner, H.-J., 2004, *Phys. Chem.*, **6**, 5007.
[41] Alexander, M. H., Capecchi, G., and Werner, H.-J., 2004, *Faraday Discuss.*, **127**, 59.
[42] Alexander, M. H., Werner, H.-J., and Manolopoulos, D. E., 1998, *J. Chem. Phys.*, **109**, 5710.
[43] Alexander, M. H., Manolopoulos, D. E., and Werner, H.-J., 2000, *J. Chem. Phys.*, **113**, 11084.
[44] Schatz, G. C., 1995, *J. Phys. Chem.*, **99**, 7522.
[45] Schatz, G. C., McCabe, P., and Connor, J. N. L., 1998, *Faraday. Discuss.*, **110**, 139.
[46] Drukker, K., and Schatz, G. C., 1999, *J. Chem. Phys.*, **111**, 2451.
[47] Whiteley, T. W. J., Dobbyn, A. J., Connor, J. N. L., and Schatz, G. C., 2000, *Phys. Chem. Chem. Phys.*, **2**, 549.
[48] Schatz, G. C., Hankel, M., Whiteley, T. W. J., and Connor, J. N. L., 2003, *J. Phys. Chem. A*, **107**, 7278.
[49] Gray, S. K., Balint-Kurti, G. G., Schatz, G. C., Lin, J. J., Liu, X., Harich, S., and Yang, X., 2000, *J. Chem. Phys.*, **113**, 7330.
[50] Hoffmann, M. R., and Schatz, G. C., 2000, *J. Chem. Phys.*, **113**, 9456.
[51] Liu, X., Lin, J. J., Harich, S., Schatz, G. C., and Yang, X., 2000, *Science*, **289**, 1536.
[52] Capecchi, G., and Werner, H.-J., 2004, *Phys. Chem. Chem. Phys.*, **6**, 4975.
[53] Balucani, N., Skouteris, D., Cartechini, L., Capozza, G., Segoloni, E., Cassavecchia, P., Alexander, M. H., Capecchi, G., and Werner, H.-J., 2003, *Phys. Rev. Lett.*, **91**, 013201.
[54] Jahn, H. A., and Teller, E., 1937, *Proc. R. Soc. London, Ser. A*, **161**, 220.
[55] Öpik, U., and Pryce, M. H. L., 1957, *Proc. Roy. Soc (London) Ser. A*, **238**, 425.
[56] Longuet-Higgins, H. C., Öpik, U., Pryce, M. H. L., and Sack, R. A., 1958, *Proc. Roy. Soc (London) Ser. A*, **244**, 1.
[57] Longuet-Higgins, H. C., 1961 *Adv. Spectrosc.*, **2**, 429.
[58] Englman, R., 1972, *The Jahn–Teller Effect in Molecules and Crystals* (New York: Wiley).
[59] Köppel, H., 1997, *Z. Phys. Chemie*, **200**, 3.
[60] Barckholtz, T. A., and Miller, T. A., 1998, *Int. Rev. Phys. Chem.*, **17**, 435.
[61] Barckholtz, T. A., and Miller, T. A., 1999, *J. Phys. Chem. A*, **103**, 2321.
[62] Bersuker, I. B., 2001, *Chem. Rev.*, **101**, 1067.
[63] Köppel, H., 2004, in *Conical Intersections: Electronic Structure, Dynamics and Spectroscopy*, edited by W. Domcke, D. R. Yarkony and H. Köppel (Singapore: World-Scientific), p. 429.
[64] Perrin, M. H., and Gouterman, M., 1967, *J. Chem. Phys.*, **46**, 1019.
[65] Zgierski, M. Z., and Pawlikowski, M., 1979, *J. Chem. Phys.*, **70**, 3444.
[66] Köppel, H., Cederbaum, L. S., and Domcke, W., 1988, *J. Chem. Phys.*, **89**, 2023.
[67] Mahapatra, S., Worth, G. A., Meyer, H.-D., Cederbaum, L. S., and Köppel, H., 2001, *J. Phys. Chem. A*, **105**, 5567.
[68] Köppel, H., Döscher, M., Bâldea, I., Meyer, H.-D., and Szalay, P. G., 2002, *J. Chem. Phys.*, **117**, 2657.
[69] Woywod, C., Scharfe, S., Krawczyk, R., Domcke, W., and Köppel, H., 2003, *J. Chem. Phys.*, **118**, 5880.
[70] Bruckmeier, R., Wunderlich Ch., and Figger, H., 1994, *Phys. Rev. Lett.*, **72**, 2250.
[71] Mahapatra, S., and Köppel, H., 1998, *J. Chem. Phys.*, **109**, 1721.
[72] Mahapatra, S., and Köppel, H., 1998, *Phys. Rev. Lett.*, **81**, 3116.
[73] Mahapatra, S., and Köppel, H., 1998, *Faraday Discuss.*, **110**, 248.
[74] Mahapatra, S., and Köppel, H., 1999, *Chem. Phys. Letters*, **306**, 387.
[75] Varandas, A. J. C., Brown, F. B., Mead, C. A., Truhlar, D. G., and Blais, N. C., 1987, *J. Chem. Phys.*, **86**, 6258.
[76] Turner, D. W., Baker, C., Baker, A. D., and Brundle, C. R., 1970, *Molecular Photoelectron Spectroscopy* (New York, Wiley).
[77] Holland, D. M. P., Karlsson, L., and Siegbahn, K., 2002, *J. Electron Spectrosc. and Related Phenomena*, **125**, 57.

[78] Venkatesan, T. S., Mahapatra, S., Cederbaum, L. S., and Köppel, H., 2004, *J. Phys. Chem. A*, **108**, 2256.
[79] Venkatesan, T. S., Mahapatra, S., Cederbaum, L. S., and Köppel, H., Unpublished results.
[80] Mahapatra, S., Vallet, V., Woywod, C., Köppel, H., and Domcke, W., 2004, *Chem. Phys.*, **304**, 17.
[81] Karlsson, L., Jadrny, R., Mattsson, L., Chau, F. T., and Siegbahn, K., 1977, *Physica Scripta*, **16**, 225.
[82] Locht, R., Leyh, B., Hoxha, A., Dehareng, D., Jochims, H. W., and Baumgärtel, H., 2000, *Chem. Phys.*, **257**, 283.
[83] Neumark, D. M., 1992, *Ann. Rev. Phys. Chem.*, **43**, 153.
[84] Neumark, D. M., 1993, *Acc. Chem. Res.*, **26**, 33.
[85] Neumark, D. M., 2001, *Ann. Rev. Phys. Chem.*, **52**, 255.
[86] Neumark, D. M., 2002, *Phys. Chem. Commun.*, **5**, 76.
[87] Metz, R. B., Bradforth, S. E., and Neumark, D. M., 1992, *Adv. Chem. Phys.*, **91**, 1.
[88] Wenthold, P. G., and Lineberger, W. C., 1999, *Acc. Chem. Res.*, **32**, 597.
[89] Weaver, A., Metz, R. B., Bradforth, S. E., and Neumark, D. M., 1989, *J. Chem. Phys.*, **90**, 2070.
[90] Mahapatra, S., Köppel, H., and Cederbaum, L. S., 1999, *J. Chem. Phys.*, **110**, 5691.
[91] Mahapatra, S., Köppel, H., Cederbaum, L. S., Stampfuss, P., and Wenzel, W., 2000, *Chem. Phys.*, **259**, 211.
[92] Weaver, A., Arnold, D. W., Bradforth, S. E., and Neumark, D. M., 1991, *J. Chem. Phys.*, **94**, 1740.
[93] Mayer, M., Cederbaum, L. S., and Köppel, H., 1994, *J. Chem. Phys.*, **100**, 899.
[94] Osborn, D. L., Leahy, D. J., Kim, E. H., de Beer, E., and Neumark, D. M., 1998, *Chem. Phys. Lett.*, **292**, 651.
[95] Klügmann, J.-S., Köppel, H., Schmatz, S., and Botschwina, P., 2003, *Chem. Phys. Lett.*, **369**, 21.
[96] Wang, X.-B., and Wang, L.-S., 2000, *J. Chem. Phys.* **113**, 10928.
[97] Krishnan, G. M., and Mahapatra, S., 2003, *J. Chem. Phys.*, **118**, 8715.
[98] Neumark, D. M., 1997, *Science*, **272**, 1446.
[99] Neumark, D. M., 2004, in *Modern Trends in Chemical Reaction Dynamics*, edited by X. Yang and K. Liu (Singapore: World Scientific), p. 453, and references therein.
[100] Ferguson, M. J., Meloni, G., Gomez, H., and Neumark, D. M., 2002, *J. Chem. Phys.*, **117**, 8181.
[101] Osterwalder, A., Nee, M. J., Zhou, J., and Neumark, D. M., 2004, *J. Chem. Phys.*, **121**, 6317.
[102] Reid, P. J., 2001, *Acc. Chem. Res.*, **34**, 691.
[103] Vaida, V., and Simon, J. D., 1995, *Science*, **268**, 1443.
[104] Davis, H. F., and Lee, Y. T., 1996, *J. Chem. Phys.*, **105**, 8142.
[105] Peterson, K. A., and Werner, H.-J., 1996, *J. Chem. Phys.*, **105**, 9823.
[106] Peterson, K. A., and Werner, H.-J., 1992, *J. Chem. Phys.*, **96**, 8948.
[107] Peterson, K. A., 1998, *J. Chem. Phys.*, **109**, 8864.
[108] Richard, E. C., and Vaida, V., 1991, *J. Chem. Phys.*, **94**, 153, 163.
[109] Reid, P. J., Esposito, A. P., Foster, C. E., and Beckman, R. A., 1997, *J. Chem. Phys.*, **107**, 8262.
[110] Sun, Z., Lou, N., and Nyman, G., 2004, *Chem. Phys. Lett.*, **393**, 204.
[111] Gilles, M. K., Polak, M. L., and Lineberger, W. C., 1992, *J. Chem. Phys.*, **96**, 8012.
[112] Stert, V., Ritze, H.-H., Nibbering, E. T. J., and Radloff, W., 2001, *Chem. Phys.*, **272**, 99.
[113] Bradforth, S. E., Arnold, D. W., Neumark, D. M., and Manolopoulos, D. E., 1993, *J. Chem. Phys.*, **99**, 6345.
[114] Schatz, G. C., Manolopoulos, D. E., Stark, K., Werner, H.-J., Arnold, D. W., Bradforth, S. E., and Neumark, D. M., 1993, *Science*, **262**, 1852.
[115] Schatz, G. C., 1993, *Science* **262**, 1828.
[116] Alexander, M. H., 2003, *J. Chem. Phys.*, **118**, 9637.
[117] Ghosal, S., and Mahapatra, S., 2004, *Chem. Phys. Lett.*, **394**, 207.

[118] Ghosal, S., and Mahapatra, S., 2005, *J. Phys. Chem. A*., **109**, 1530.
[119] Rebentrost, F., and Lester, W. A. J. Jr, 1975, *J. Chem. Phys*., **63**, 3737.
[120] Rebentrost, F., and Lester, W. A. Jr, 1976, *J. Chem. Phys*., **64**, 3879.
[121] Rebentrost, F., and Lester, W. A. Jr, 1976, *J. Chem. Phys*., **64**, 4223.
[122] Manolopoulos, D. E., and Alexander, M. H., 2004, *Phys. Chem. Chem. Phys*., **6**, 4984.
[123] Mahapatra, S., Köppel, H., and Cederbaum, L. S., 2001, *J. Phys. Chem. A*, **105**, 2321.
[124] Wu, Y.-S. M., Kuppermann, A., and Lepetit, B., 1991, *Chem. Phys. Lett*., **186**, 319.
[125] Wu, Y.-S. M., and Kuppermann, A., 1993, *Chem. Phys. Lett*., **201**, 178.
[126] Kendrick, B. K., 2000, *J. Chem. Phys*., **112**, 5679.
[127] Juanes-Marcos, J. C., and Althorpe, S. C., 2003, *Chem. Phys. Lett*., **381**, 743.
[128] Aoiz, F. J. *et al*., 2002, *J. Chem. Phys*., **116**, 10692.
[129] Sayós, R., Oliva, C., and González, M., 2002, *J. Chem. Phys*., **117**, 670.
[130] González, M., Oliva, C., and Sayós, R., 2002, *J. Chem. Phys*., **117**, 680.
[131] Skouteries, D., Manolopoulos, D. E., Bian, W., Werner, H.-J., Lai, L.-H., and Liu, K., 1999, *Science*, **286**, 1713.
[132] Ghosal, S., and Mahapatra, S., 2004, *J. Chem. Phys*., **121**, 5740.